



OPEN

A gelation transition enables the self-organization of bipolar metaphase spindles

Benjamin A. Dalton ^{1,2,3,4,5}, David Oriola ^{1,2,3,4,5}, Franziska Decker ^{1,2,3,4,5}, Frank Jülicher ^{2,3,4} ✉ and Jan Brugués ^{1,2,3,4} ✉

The mitotic spindle is a highly dynamic bipolar structure that emerges from the self-organization of microtubules, molecular motors and other proteins. Sustained motor-driven poleward flows of dynamic microtubules play a key role in the bipolar organization of spindles. However, it is not understood how the local activity of motor proteins generates these large-scale coherent poleward flows. Here we show that a gelation transition enables long-range microtubule transport causing the spindles to self-organize into two oppositely polarized microtubule gels. Laser ablation experiments reveal that local active stresses generated at the spindle midplane propagate through the structure, thereby driving global coherent microtubule flows. Simulations show that microtubule gels undergoing rapid turnover can exhibit long stress relaxation times, in agreement with the long-range flows observed in experiments. Finally, our model predicts that in the presence of branching microtubule nucleation, either disrupting such flows or decreasing the network connectivity can lead to a microtubule polarity reversal in spindles. We experimentally confirm this inversion of polarity by abolishing the microtubule transport in spindles. Overall, we uncover a connection between spindle rheology and architecture in spindle self-organization.

Cells use active cytoskeletal structures to perform essential processes such as cell division, cell motility, force generation and morphogenesis^{1,2}. Cytoskeletal structures consist of dynamic filaments that are cross-linked by molecular motors and rely on constant energy consumption for their assembly and function. Molecular motors drive the organization of cytoskeletal structures by actively clustering, pulling and sliding filaments apart^{3–6}. This activity often leads to the emergence of large-scale flows within the structures that can transport material⁷, exert force⁸ or establish a gradient of filament polarity⁹. Although the emergence of flows in active matter has been successfully captured by hydrodynamic theories¹⁰, the microscopic origins of flows and their relation to the rheology and architecture of cellular structures remains poorly understood.

A prominent example of active large-scale flows is the poleward movement of microtubules observed in metaphase spindles^{11,12}. Spindles are self-organized molecular machines responsible for the segregation of sister chromatids during cell division. They are made of dynamic microtubules that are continuously transported towards the poles by molecular motors in a process known as poleward flux³. In *Xenopus laevis* egg extract spindles, this flux depends on the activity of Eg5—a kinesin motor that can slide antiparallel microtubules^{3,13–15}. Spindle bipolarity is known to be a consequence of Eg5 motors cross-linking and forcing apart microtubules of opposite polarities, thereby sorting microtubules into an antiparallel array¹⁶. Mean-field models considering such a mechanism naturally lead to a linear dependence of velocity on the spatial distribution of antiparallel microtubule overlaps or polarity field^{15,17}, which contrasts with the remarkably constant flows observed in spindles¹⁸ where the density of antiparallel microtubule overlaps forms a pronounced gradient⁹.

Recent work in vitro demonstrated that mixtures of stabilized microtubules and motors can generate active flows that are

independent of the spatial distribution of antiparallel microtubule overlaps¹⁷. It was suggested that these flows can arise from the high degree of connectivity introduced by molecular motors. However, in contrast to stabilized mixtures, microtubules in the spindle turnover rapidly^{19–21} and are constantly nucleated throughout the structure^{22,23}. In particular, microtubule nucleation is an autocatalytic process^{23–25}, which leads to microtubule structures that are genuinely different from the ones obtained in other simplified in vitro systems^{6,17,26}. Previous attempts to recapitulate such flows using computational models lacked some key aspects such as microtubule dynamics²⁷ or the polarity-preserving effect of branching microtubule nucleation²⁸. How the interplay between microtubule active flows and autocatalytic microtubule waves establish the correct spindle architecture remains unknown.

Here we combine experiments and simulations to show that a gelation transition enables long-range active flows in *Xenopus* egg extract spindles. This transition leads to the self-organization of two polar, interpenetrating and mechanically distinct microtubule gels of opposite polarity. Simulations of highly cross-linked active microtubule networks reveal that despite continuous microtubule turnover, microtubule gels can sustain long-range steady-state flows. Furthermore, simulations predict that either disrupting such flows or decreasing the network connectivity can lead to a microtubule polarity reversal in spindles. We experimentally confirm our prediction by disrupting Eg5 activity and abolishing flows in spindles. Altogether, we illustrate a functional relevance of gelation in the proper organization of metaphase spindles, elucidating an unexpected connection between gelation, microtubule nucleation and microtubule transport.

Active flows in the spindle are independent of polarity

The mechanism by which Eg5 motors sort antiparallel overlaps implies that forces between microtubule pairs should strongly

¹Max Planck Institute of Molecular Cell Biology and Genetics, Dresden, Germany. ²Max Planck Institute for the Physics of Complex Systems, Dresden, Germany. ³Center for Systems Biology Dresden, Dresden, Germany. ⁴Cluster of Excellence Physics of Life, TU Dresden, Dresden, Germany. ⁵These authors contributed equally: Benjamin A. Dalton, David Oriola, Franziska Decker. ✉e-mail: julicher@pks.mpg.de; bruges@mpi-cbg.de

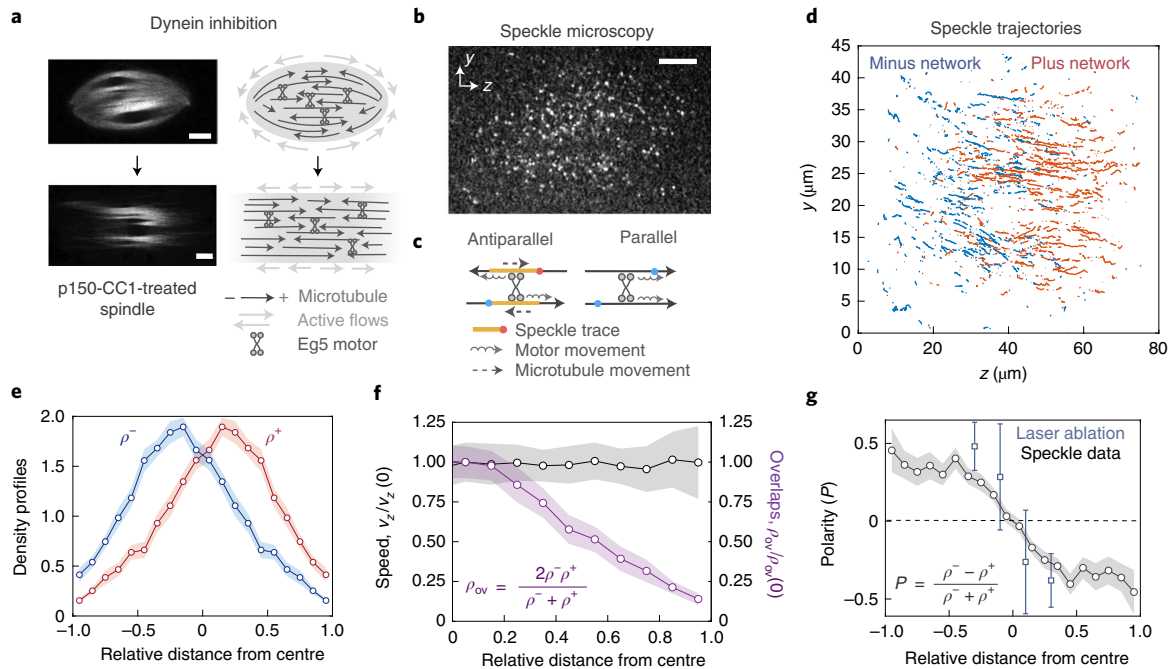


Fig. 1 | Local sorting of antiparallel microtubule overlaps is not sufficient to explain poleward microtubule transport. **a**, Fluorescent spindles labelled with Atto565 pig tubulin and corresponding schematic of the spindle architecture for the control and dynein-inhibited cases. Scale bar, 10 μm . **b**, Speckle microscopy (-1 nM Atto565 frog tubulin) is used to measure the microtubule transport (Supplementary Video 2). Scale bar, 10 μm . **c**, Speckles move in antiparallel overlaps due to the action of Eg5 motors, but they remain static in parallel overlaps. **d**, Speckle trajectories are tracked and classified according to their direction of motion. Speckles whose longitudinal velocity was smaller than $0.2 \mu\text{m min}^{-1}$ were discarded from the analysis (~4%). The total time elapsed is 210 s. **e**, Number density of the two microtubule populations, namely, ρ^+ and ρ^- , for the plus and minus networks, respectively (mean \pm s.d.; $n=10$ spindles). **f**, Normalized value of the averaged velocity profiles of the plus and minus networks $v_z/v_z(0)$ compared with the normalized number density of antiparallel overlaps $\rho_{ov}/\rho_{ov}(0)$ (Supplementary Information). Eg5 can only generate forces in the spindle centre where antiparallel overlaps are enriched (mean \pm s.d.; $n=10$ spindles). **g**, Comparison between the polarity profile $P=(\rho_- - \rho_+)/(\rho_- + \rho_+)$ obtained from the speckle data (mean \pm s.d.; $n=10$ spindles) and the polarity profile obtained using laser ablation (mean \pm s.d.; $n=25$ cuts). This result provides direct evidence that the direction of movement of the speckles is a readout of the microtubule polarity.

depend on their relative orientation^{15,16}. In this picture, antiparallel interactions drive the motion of both filaments, whereas parallel filaments remain static¹⁶. A mean-field description would result in flows that linearly depend on the antiparallel microtubule overlap density^{15,17}. To test this mechanism in *Xenopus* spindles, we quantified the microtubule transport and density of antiparallel overlaps throughout the spindle structure, similar to previous studies^{14,18}. To focus on microtubule transport, we inhibited dynein activity, which is known to affect poleward flux at the poles as well as control spindle shape^{14,18,29} (Fig. 1, Extended Data Fig. 1a and Supplementary Video 1). Therefore, we treated spindles with p150-CC1 (which disrupts pole formation), causing microtubule alignment along the spindle long axis (Fig. 1a)³⁰. Dynein inhibition only caused a minor effect on the spindle architecture (Extended Data Fig. 1b–d). To visualize the motion of individual microtubules in the spindles, we used single-molecule speckle microscopy^{9,18} (Fig. 1b,c and Supplementary Video 2). Speckle trajectories showed two distinct populations (Fig. 1d) moving coherently towards the poles. To compare the microtubule velocity profiles with the antiparallel microtubule overlaps, we quantified the density distribution of the two microtubule populations ρ_+ and ρ_- (Fig. 1e), revealing two interpenetrating networks, in agreement with previous studies¹⁸. Computing the density of microtubule overlaps as $\rho_{ov} = 2\rho_-\rho_+/(\rho_- + \rho_+)$, we found that the number density of antiparallel overlaps was maximal at the spindle centre and decreased by ~90% at the poles (Fig. 1f). In contrast, microtubule transport was found to be constant throughout the spindle with an average value of $2.5 \pm 0.4 \mu\text{m min}^{-1}$ ($n=549$ speckles from 10 spindles; mean \pm s.d.; Fig. 1f and Extended Data Fig. 1a),

in agreement with Yang et al.¹⁸. To ensure that speckle microscopy provides an accurate readout of microtubule polarity, we compared $P=(\rho_- - \rho_+)/(\rho_- + \rho_+)$ (Fig. 1g, circles) with the microtubule polarity profiles obtained by laser ablation (Fig. 1g, squares) (Methods and Brugués et al.⁹). The two approaches were in agreement, confirming that the direction of speckle transport reveals the microtubule polarity. We conclude that the microtubule transport velocity is independent of the local antiparallel overlap density (that is, the microtubule polarity; Extended Data Fig. 2). Thus, a local mean-field picture of antiparallel sliding is not sufficient to explain the long-range flows.

Active flows are a consequence of long-range stress propagation

Our speckle analysis suggests that a local mean-field picture of antiparallel sliding (hereafter referred to as ‘local sorting’) is not sufficient to explain microtubule transport in spindles. One possible explanation for the polarity-independent flows observed throughout the spindle is that the local stresses generated by Eg5 in the region of antiparallel overlaps are propagated over long distances. To test this hypothesis, we designed an assay combining fluorescent speckle microscopy and laser ablation (Fig. 2a and Methods). We reasoned that if Eg5 activity is mainly restricted to the spindle midplane and propagates throughout the structure, disconnecting a region of the spindle that is far from the midplane using laser ablation should reduce microtubule transport within that disconnected region (DR; Fig. 2a(i)). Alternatively, if Eg5 is homogeneously acting in the structure via local sorting, microtubule motion in the

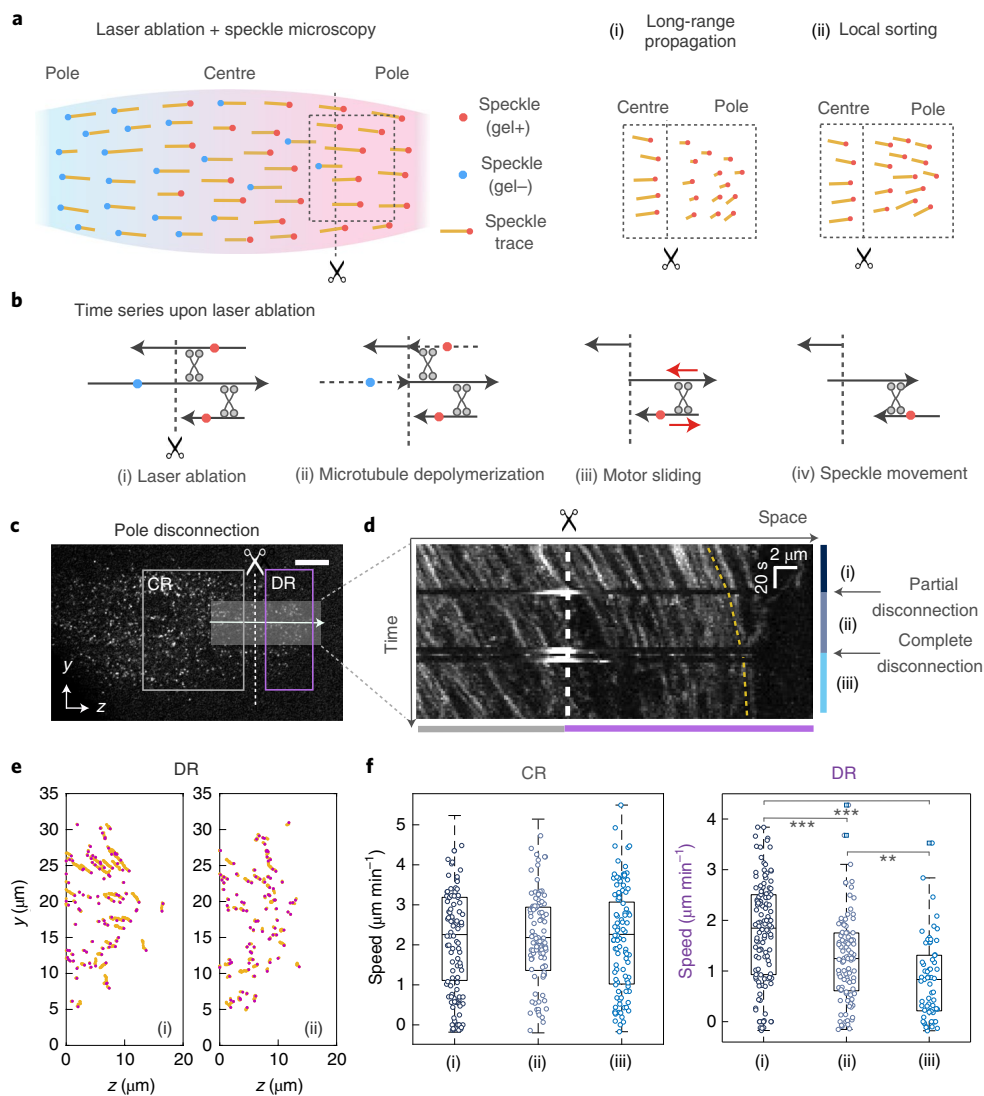


Fig. 2 | Microtubule transport is a consequence of long-range stress propagation mediated by Eg5. **a**, Combination of laser ablation and speckle microscopy techniques are used to distinguish between two scenarios: (i) Eg5 generates stresses at the centre of the spindle and they propagate across the structure. Speckles stop in the pole region after laser ablation, whereas speckles in the rest of the spindle remain unaffected. (ii) Eg5 generates local stresses throughout the structure and speckles are not affected in the pole region after the cut. **b**, Antiparallel overlaps in the DR that survive after the laser cut are the only ones that can drive the poleward speckle movement. **c**, Fluorescent speckle image before laser ablation. Scale bar, 10 μm . CR, connected region; DR, disconnected region. The arrow denotes the direction along which the kymograph in **d** is studied and the width of the grey region denotes the averaged region. **d**, Kymograph from **c** showing how speckle trajectories stop in the DR after consecutive laser ablation events. The kymograph is divided in three different time intervals, namely, (i), (ii) and (iii), between the laser cuts. The fact that the speckles stop on disconnection of the pole validates the scenario in **a**(i). **e**, Speckle trajectories before (time interval (i)) and after (time interval (ii)) the first laser ablation during 40 s (Supplementary Videos 4 and 5). **f**, On-axis velocity of speckles during time intervals (i), (ii) and (iii) in the CR and DR. A progressive reduction in speckle velocity is observed in the DR, whereas the speckle velocity remains unaffected in the CR. Only speckles with $> -0.2 \mu\text{m min}^{-1}$ were considered in the analysis. A reduced subset of 100 data points is shown in the CR case for the sake of clarity. $**P < 0.01$ and $***P < 0.001$. The squares indicate outliers. A two-sample *t*-test was used.

DR should mainly remain unaffected (Fig. 2a(ii)). A key aspect of this perturbation is that the poleward-moving speckles that survive after the laser cut would correspond to intact antiparallel overlaps, since the cut microtubules only depolymerize from the newly created plus end, whereas the new minus ends remain stable⁹ (Fig. 2b). Additionally, kinetochore microtubules connecting the poles to the midplane will depolymerize in the DR, thus not contributing to the analysis.

We achieved the complete disconnection of a spindle pole by a series of three consecutive laser cuts across the spindle (Fig. 2a–c and Supplementary Video 3). After each series of cuts (Fig. 2d,

white sparks), all the speckles in the severed region instantaneously slowed down (Fig. 2d–f and Supplementary Video 3). We analysed the corresponding time intervals labelled (i), (ii) and (iii) (Fig. 2d–f) between the successive laser cuts. The microtubule velocity was significantly reduced after ablation in the DR from $1.8 \pm 0.1 \mu\text{m min}^{-1}$ (time interval (i); $n = 122$ trajectories; median \pm s.e.m.) before the cut to $0.8 \pm 0.1 \mu\text{m min}^{-1}$ after the cuts (time interval (iii); $n = 61$ trajectories; mean \pm s.e.m.) (Fig. 2d–f and Supplementary Videos 4–6). In contrast, the microtubule velocity remained unaffected in the connected region (CR) (Fig. 2d,f and Supplementary Videos 7–9). The instantaneous slow down of the speckles after a series of

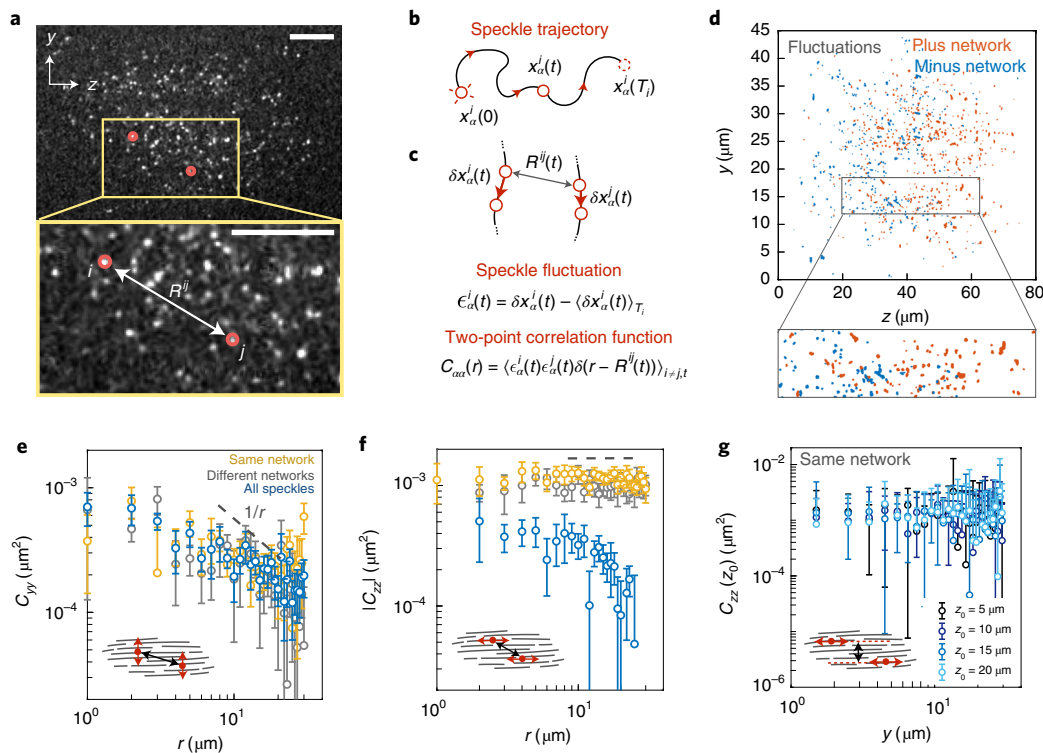


Fig. 3 | Two-point correlations reveal two interacting rigid-like microtubule networks in the spindle. **a**, Fluorescently labelled tubulin speckles in a dynein-inhibited spindle. Zoomed-in region shows the speckle pair (i, j) separated by distance R^{ij} . Scale bar, 5 μm . **b**, Speckle trajectory tracked from its appearance at $t=0$ and disappearance at time $t=T_i$. The position of speckle i at time t is defined as $x_\alpha^i(t)$ during its lifetime $t \in [0, T_i]$, where $\alpha=z$ and $\alpha=y$ correspond to the longitudinal and transversal components, respectively. **c**, Speckle-pair trajectories and positions at two different times separated by Δt . A speckle fluctuation is defined as $e_\alpha^i(t) = \delta x_\alpha^i(t) - \langle \delta x_\alpha^i(t) \rangle_{T_i}$, where $\delta x_\alpha^i(t) = x_\alpha^i(t + \Delta t) - x_\alpha^i(t)$. The two-point correlation function is defined as $C_{\alpha\alpha}(r) = \langle e_\alpha^i(t) e_\alpha^j(t) \delta(r - R^{ij}(t)) \rangle_{i \neq j, t}$. **d**, Speckle fluctuations and classification according to their mean velocity along the spindle long axis z . Speckles moving towards the right are coloured in red, whereas speckles moving towards the left are coloured in blue. The total time elapsed is 210 s. **e–g**, Log-log plots of the two-point correlations for dynein-inhibited spindles (mean \pm s.d.; $n=10$ spindles), namely, $C_{yy}(r)$ (**e**) and $|C_{zz}(r)|$ (**f, g**), of the speckles classified in the same network (yellow), different networks (grey) or not classified (blue) (Supplementary Information). The absolute value of C_{zz} is used to compare the amplitude of longitudinal correlations using speckles from the same and different networks, despite correlations having the opposite sign. Transversal fluctuations decay and are decoupled between the two networks, whereas longitudinal correlations are coupled between the networks and do not decay within the networks. **g**, Shear correlations $C_{zz}(y, z_0) = \langle e_z^i(t) e_z^j(t) \delta(y - Y^{ij}(t)) \delta(z_0 - Z^{ij}(t)) \rangle_{i \neq j, t}$ for $z_0 = 5, 10, 15$ and $20 \mu\text{m}$ (from dark to light blue) (Supplementary Information).

cuts indicates that connectivity is essential to sustain the poleward flux at the poles. The residual flux after complete disconnection is probably attributed to a minor local sorting contribution at the pole, which is non-zero (Fig. 1f,g) due to the remaining antiparallel overlap. We obtained similar results in other experiment replicas (Extended Data Fig. 3 and Supplementary Videos 10 and 11). We also note that most of the speckles in the DR survived after the complete disconnection of the pole (Fig. 2d and Supplementary Video 6), indicating that microtubules in the pole region are typically short, in agreement with previous studies⁹. However, we cannot dispel the likelihood that some long microtubules extend into the pole region, thus contributing to the flux. Regardless, the reduction in transport in the DR after ablation suggests that microtubule flux in that region is not a consequence of local microtubule sorting or treadmilling at the spindle poles, as previously proposed^{19,31,32}. Instead, local stresses generated by Eg5 propagate throughout the structure from the spindle midplane region to the poles, driving microtubules poleward.

The spindle consists of two rigid-like microtubule networks

We wondered how the two microtubule populations in the spindle could sustain long-range stress propagation, especially given that microtubules are—on average—short compared with the length of

the spindle and that they turnover rapidly^{9,19}. To gain an insight into the material properties of the two networks, we measured the fluctuations of speckle pairs in dynein-inhibited spindles (Fig. 3a–d) and performed a two-point correlation analysis on these fluctuations (Fig. 3e–g) (Methods and refs. 33,34). We calculated two-point correlations $C_{\alpha\alpha}(r)$ along the transversal ($\alpha=y$) and longitudinal ($\alpha=z$) axes of the spindle as a function of the distance between speckles, r (Fig. 3b,c). We classified the speckles according to their direction of movement and considered three different cases: pairs belonging to the same network, pairs from different networks and pairs taken indiscriminately from either population (Fig. 3e–g, with yellow, grey and blue colours, respectively). Transversal correlations decayed as $\sim 1/r$ (Fig. 3e), in agreement with correlations expected for a continuum material^{33,34}. Strikingly, when we considered speckle pairs from either a single network or different networks, we did not observe any decay in the longitudinal correlations (Fig. 3f, yellow and grey). This suggests that the two networks behave as rigid-like materials along the spindle long axis and they are deformable along the short axis. The fluctuations in speckle pairs coming from the same network were positively correlated, implying coherent stress transmission across each network. In contrast, the fluctuations in speckle pairs from opposite networks were negatively correlated, suggesting that Eg5 acts on the two networks pushing them apart.

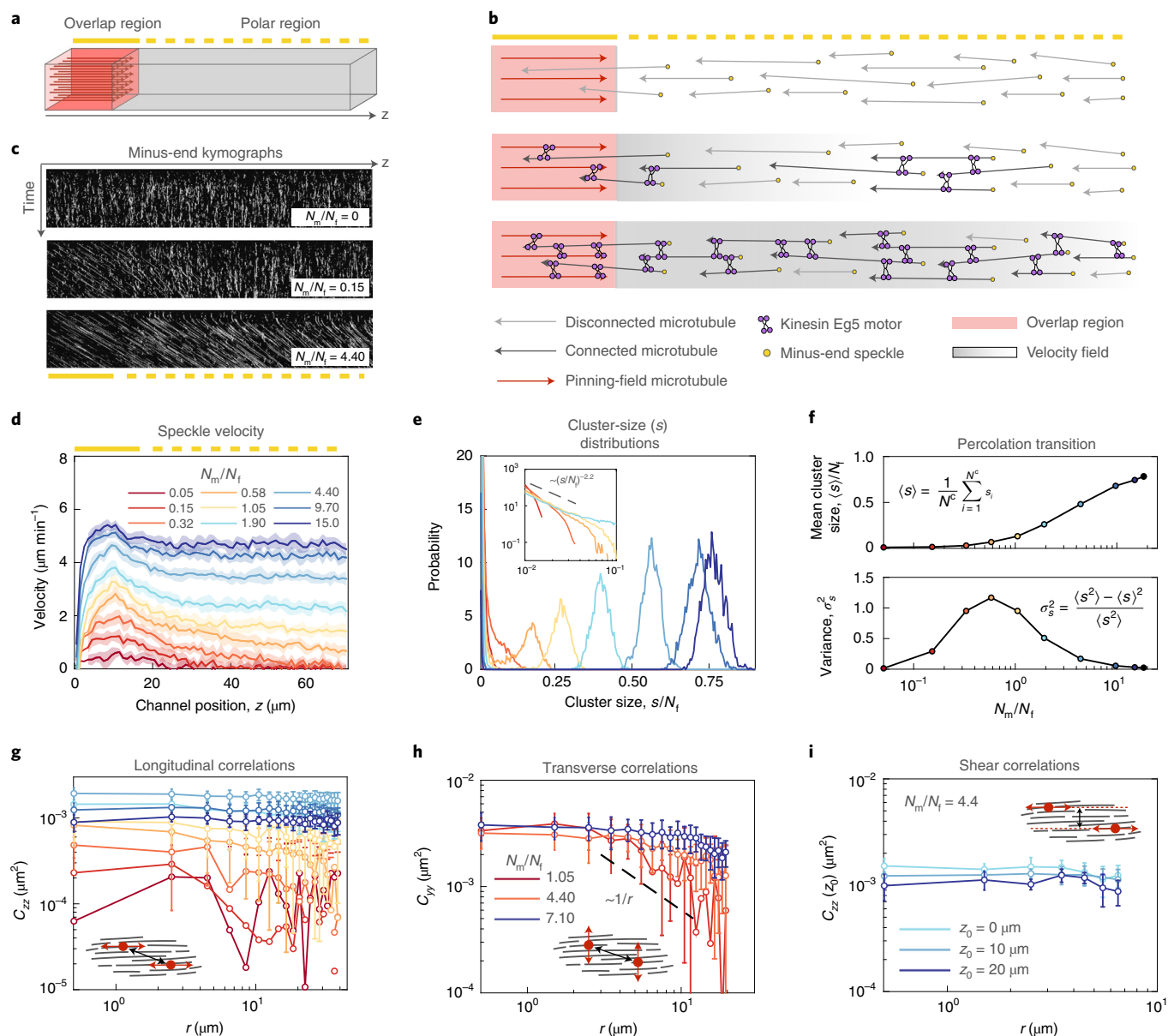


Fig. 4 | A gelation transition enables long-range flows in filament networks. Computer simulations of filament networks in a pinning-field channel. **a**, The pinning field substitutes for one of two filament networks. The schematic shows the simulation environment of the pinning-field channel. **b**, Conceptual overview for simulations: dynamic microtubules nucleate throughout the channel, restricting antiparallel overlaps to the pinning-field region. Increasing the Eg5 concentration increases the filament connectivity, enabling long-range flow. The solid walls constrain the filament orientations and maintain a high filament density. **c**, Kymograph for minus-end speckles, showing a line section along the channel long axis for three different Eg5 concentrations (Supplementary Video 12); here N_m is the number of motors and N_f is the number of filaments. **d**, Length scale of the filament velocity profiles increases with increasing Eg5 concentration (figure legend shows the colour scheme for **d**, **e** and **g**) (mean \pm s.d.; $n=10$ simulations). **e**, Distributions $P(s/N_f)$ of filament cluster size s/N_f indicate a percolation transition in the filament networks. The distributions are calculated as a function of Eg5 concentration. Inset, near the percolation threshold, the distribution approaches a power-law distribution with an exponent of -2.2 , in agreement with the percolation theory. **f**, Mean and normalized variance for the cluster-size distributions in **e**. Here s_i is the size of the i th cluster, N^c is the total number of clusters and n is the upper cluster size. **g**, Longitudinal two-point fluctuation correlations C_{zz} reveal the onset of rigid-like behaviour in gelled networks. The correlations are shown for simulations in **d**, **e** and **f**. **h**, Transverse two-point correlations C_{yy} decay for high Eg5 concentrations. A wider simulation domain is used to probe transverse fluctuations (Methods). **i**, Shear correlations $C_{zz}(z_0)$ for gelled networks are also constant over a range of z_0 values. The channel geometry is the same as in **h**.

Similar results were obtained when studying the shear correlations (Fig. 3g). These results suggest that the spindle is composed of two interpenetrating rigid-like microtubule networks of opposite polarity that are coupled at the central overlap region and driven apart by Eg5 activity.

A gelation transition enables long-range stress propagation

Mixtures of filaments and motors can behave like fluids or gels depending on the filament connectivity^{35–37}. To test whether a gelation transition underlies the long-range propagation of stresses

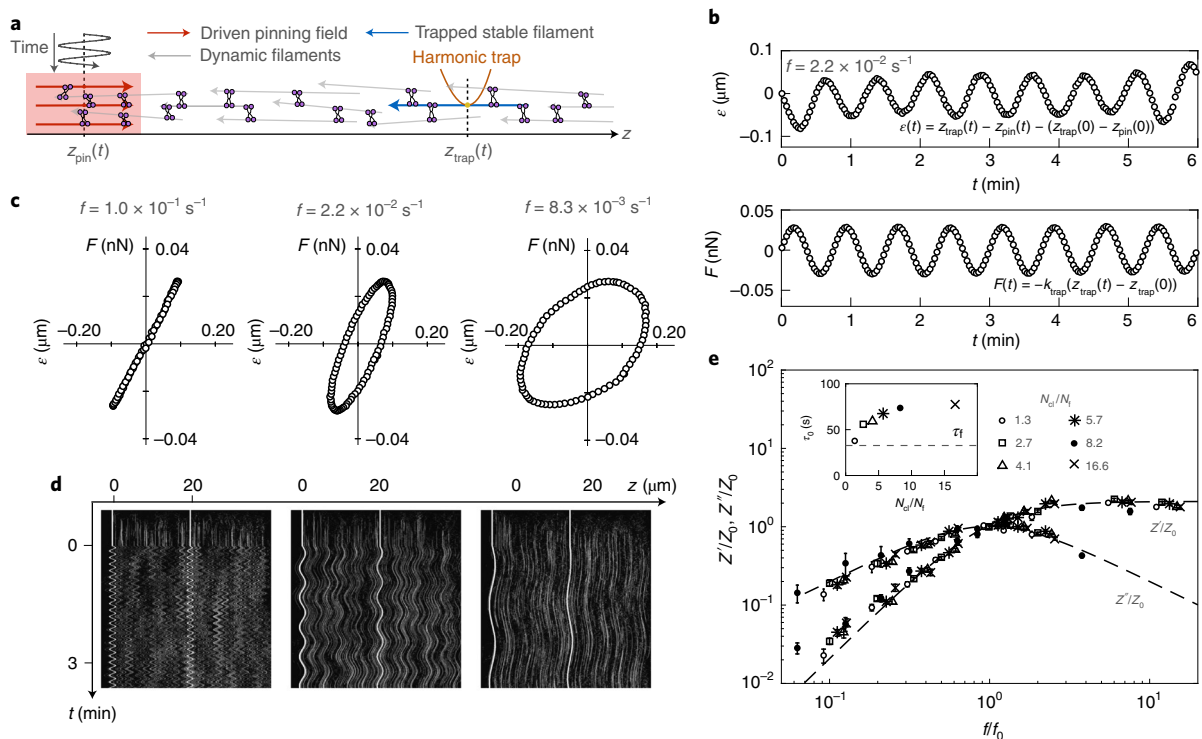


Fig. 5 | Viscoelastic relaxation time of the gel is larger than filament lifetime. Active microrheology measurements for viscoelastic response in simulated filament networks. **a**, Schematic showing the active microrheology setup, including an oscillating pinning field and a trapped probe filament. The permanent probe filament is confined to a harmonic trap in the x , y and z axes, set at $z_{\text{trap}} = 20 \mu\text{m}$. The pinning field oscillates according to $z_{\text{pin}}(t) = z_0 \sin(2\pi ft)$, where $z_0 = 0.75 \mu\text{m}$. Network connectivity enables stress propagation from the pinning field to the trapped probe filament. Given that motors only generate forces at the pinning field and effectively act as passive cross-linkers elsewhere, the motor activity was turned off. The parameters for passive cross-linkers are listed in Supplementary Information. **b**, Network deformations are driven by pinning-field oscillations and resistance of the trapped filament. The network deformations are given by $\epsilon(t) = z_{\text{trap}}(t) - z_{\text{pin}}(t) - L_0$, where $L_0 = 20 \mu\text{m}$. The trajectories of probe filaments indicate the force response; k_{trap} is the stiffness of the harmonic trap. **c**, Phase plots show that contributions from viscous and elastic responses vary depending on the driving frequency. The phase response is shown for three frequencies ($N_c/N_f \approx 4$). **d**, Kymographs for gelled networks show the probe moving in response to the driven pinning field. The driving frequencies are the same as in **c**. **e**, Viscoelastic transition times vary depending on the cross-linker concentration. The plot shows the rescaled material viscoelastic response over a range of cross-linker concentrations ($n = 10$ simulations; mean \pm s.d.), rescaled by the crossover frequency f_0 and crossover modulus Z_0 . The fit for a Maxwell model included for $Z'/Z_0 = A' (f/f_0)^2 / (1 + (f/f_0)^2)$ and $Z''/Z_0 = A'' (f/f_0) / (1 + (f/f_0)^2)$, where $A' = 2.10$ and $A'' = 2.01$. Inset, viscoelastic relaxation times τ_0 increase with increasing cross-linker concentration (defined as the number of cross-linkers N_c per number of filaments N_f); τ_f corresponds to the mean filament lifetime.

in the spindle, we turned to large-scale simulations (Methods, Supplementary Information and Extended Data Fig. 4). For simplicity, we simulated the dynamics of one filament network and substituted the second network for a pinning-field structure of fixed, polar aligned filaments. We also included active motor cross-links and filament turnover. The length of the fixed arrangement of filaments controlled the region of antiparallel overlaps, representing the spindle midplane (Fig. 4a,b, red region).

To study the effect of connectivity on transport, we systematically varied the number of motors in the system (Fig. 4c and Supplementary Video 12). We found that for motor concentrations below 0.5 motors per filament, the flows abruptly decayed beyond the overlap region with a length scale close to the mean filament length (Fig. 4d). Above this concentration, we observed the emergence of coherent flows that spanned the entire channel (up to a range that was approximately ten times larger than the mean filament length). To test if the emergence of these long-range flows corresponds to the onset of a gelation transition, we measured the connectivity within the cross-linked filament networks and calculated the distribution of cluster sizes as a function of motor concentration (Fig. 4e). At approximately 0.5 motors per filament, we observed the emergence of a distinct peak in the cluster-size distribution accompanied by a maximum in the cluster-size variance

(Fig. 4f), indicating that the system undergoes a percolation transition. The peak in the cluster-size distribution indicates the formation of a filament cluster that spans the entire length of the channel, enabling the long-range propagation of stresses generated at the pinning field. The size of the dominant cluster increases as a function of motor concentration, saturating for highly cross-linked networks (10–15 motors per filament^{17,34}). Adding a second population of passive cross-linkers led to an increase in the length scale of the velocity profile as well as reducing the peak flow due to an increase in the friction in the pinning-field region (Extended Data Fig. 4e).

Finally, we tested whether gelation could account for the material properties of the spindle by performing two-point microrheology in our simulations. For gelled systems, longitudinal correlations were long-range, transversal correlations decayed as $\sim 1/r$, and there were no shear fluctuations (Fig. 4g–i), in agreement with experiments (Fig. 3e,f, yellow curves, and Fig. 3g). Altogether, our simulations show that a gelled polar network is sufficient to sustain the long-range flows observed in spindles.

Polar gels exhibit long relaxation times despite filament turnover

Our experiments and simulations suggest that the gelation of microtubule networks in spindles results in the emergence of two

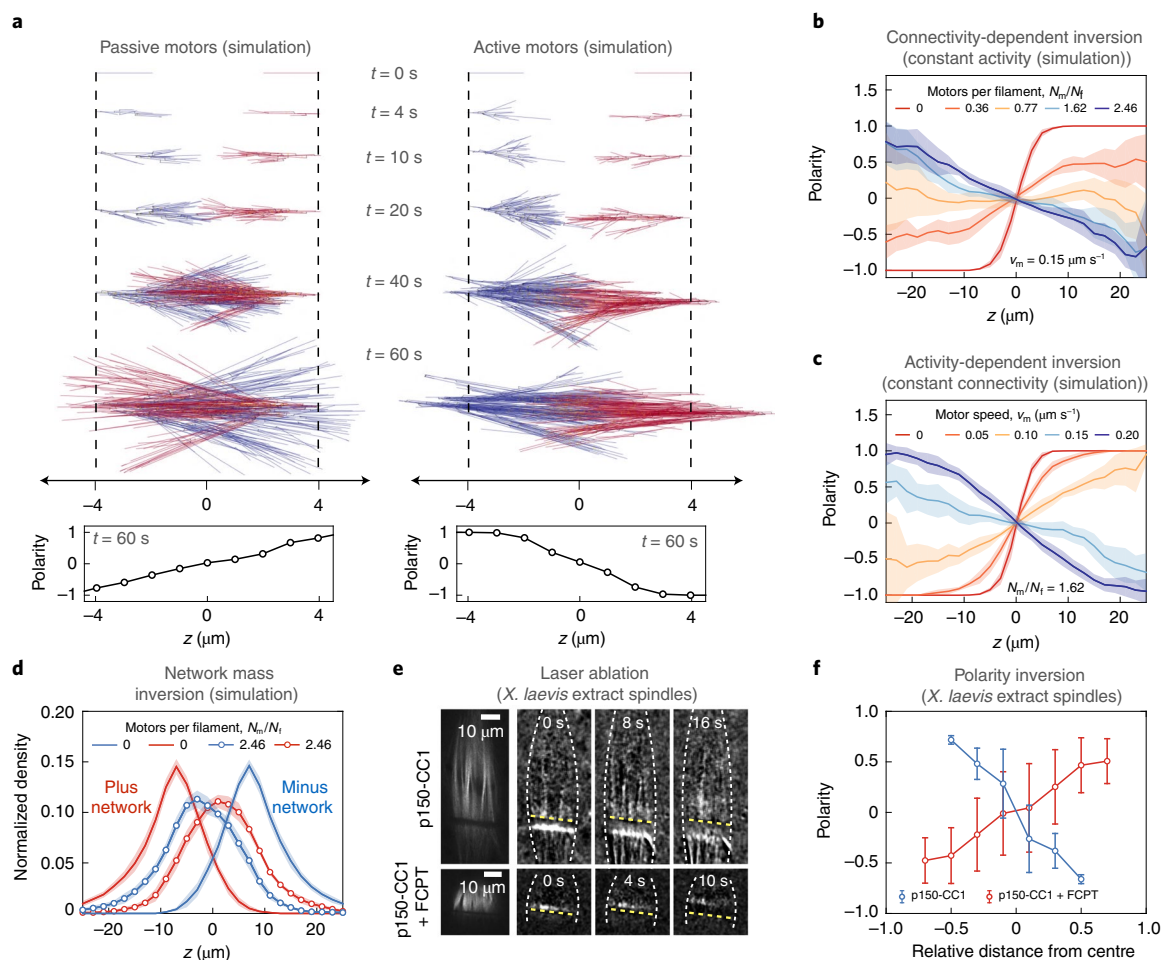


Fig. 6 | Microtubule gelation is required for the proper spindle architecture. **a**, Computer simulations reveal a mechanism for generating polarity profiles observed in p150-CC1-treated *Xenopus* extract spindles. The simulation snapshots show the time evolution of two branching filament networks, interacting via passive or active motors. In passive systems, the polarity profiles are reversed compared with the polarity observed in spindles. In active systems, local polarity sorting and gelation lead to the establishment of the proper spindle polarity, with transport counteracting the effect of the autocatalytic branching wave. **b**, Polarity reversal enabled by gelation in active systems (steady state at $t = 12$ min and constant $v_0^k = 0.15 \mu\text{m s}^{-1}$). Varying connectivity by the Eg5 population size ($N_{\text{cl}}/N_{\text{MT}} = 0, 0.36, 0.77, 1.60$ and 2.50 from red to blue), where N_m is the number of motors, N_f is the number of filaments and v_m is the motor speed. **c**, Polarity reversal enabled by activity in gelled networks ($t = 12$ min and constant $N_{\text{cl}}/N_{\text{MT}} = 1.62$). Varying the activity by unloaded Eg5 velocity ($v_0^k = 0, 0.10, 0.15$ and $0.20 \mu\text{m s}^{-1}$ from red to blue). **d**, Gelation enables proper organization of the two networks ($v_0^k = 0.15 \mu\text{m s}^{-1}$). In **b–d**, branching nucleation occurs between $z = -8 \mu\text{m}$ and $8 \mu\text{m}$ (Supplementary Information) and $n = 10$ simulations with mean \pm s.d. **e**, Laser ablation for dynein-inhibited spindles in the presence (Supplementary Videos 15 and 16) and absence (Supplementary Videos 17 and 18) of FCPT. Time series of differential intensity plots show depolymerization waves travelling in opposite directions, indicating a microtubule polarity reversal. **f**, Polarity reversal in *Xenopus* extract spindles measured using laser ablation (mean \pm s.d.; $n = 39$ cuts; red circles). The blue circles correspond to the laser ablation data in Fig. 1g.

interpenetrating gels. However, the binding and unbinding of motor proteins and rapid microtubule turnover should fluidize the gels at long timescales³⁸. To understand the rheological properties of polar filament gels, in the absence of motor activity, we oscillated the pinning field and studied the response of a filament probe trapped in a harmonic potential far from the pinning field (Fig. 5a–c). We measured the response of the probe to frequencies in the range of ~ 0.003 – 0.100 s^{-1} . This method mimics previous microrheological measurements using a combination of rigid and flexible microneedles in spindles³⁸, although in those measurements, the two gels were indistinguishable. To characterize the rheological properties of the network, we calculated the in-phase and out-of-phase response of the network deformation, namely, Z' and Z'' , respectively, to periodic forcing (Supplementary Information and Extended Data Fig. 5a). In the moderately cross-linked regime and at higher frequencies (0.1 s^{-1}), the response of the trapped filament was in phase

with the deformations, implying that the gel behaved as an elastic solid (Fig. 5c, left). In contrast, for lower frequencies (0.008 s^{-1}), the response was out of phase and the system behaved as a viscous fluid (Fig. 5c, right). The crossover frequency from the elastic to fluid response varied with the cross-linker concentration (Extended Data Fig. 5a). However, by rescaling Z' , Z'' and frequency with respect to the corresponding values at the crossover point for different cross-linker concentrations, we found that all the curves collapsed following a Maxwell model (Fig. 5e). The relaxation time increases with increasing cross-linking and saturates for ~ 10 cross-links per microtubule (Fig. 5e, inset). Strikingly, for high cross-linker concentrations, the relaxation time is $\sim 80 \text{ s}$, which is approximately three to four times larger than the mean filament lifetime. This relaxation time scale depends on the microtubule-length distribution as well as the cross-linker binding/unbinding kinetics (Extended Data Fig. 5d). Finally, for moderately cross-linked networks

(~5 cross-linkers per microtubule), we estimated the hydrodynamic length scale to be ~300 μm , which is much larger than the channel length (Supplementary Information and Extended Data Fig. 5c,d). Thus, we conclude that long-range stress propagation in the spindle is a consequence of a long relaxation time, despite the fast microtubule turnover, emerging from network gelation.

Microtubule gelation controls a polarity-reversal transition

Our results show that above the gelation point, flows become long range and independent of the filament polarity profile, whereas below the gelation point, flows decay over the length scale of a filament. We reasoned that long-range, polarity-independent flows may be required to maintain the proper spindle polarity. Indeed, microtubule transport is necessary to counteract branching microtubule nucleation in spindles, which is known to occur in the form of autocatalytic waves that propagate away from the mother microtubules^{22,23,25,39,40}. To test this, we simulated spindles by considering two interacting networks of opposite polarity. We included microtubule branching nucleation and we systematically varied the connectivity in the network as well as motor activity (Fig. 6a–d, Extended Data Figs. 6 and 7, and Supplementary Information). Above the gelation point and for a sufficiently large motor activity, we observed the emergence of a gradient of polarity at the steady state similar to those observed in experiments (Fig. 6a and Supplementary Video 13), and with network densities having the same organization as in real spindles (Fig. 6d compared with Fig. 1e). Strikingly, when we reduced the connectivity below the gelation point and kept the motor activity constant, filaments self-organized with a reversed polarity profile, with autocatalytic waves of filaments growing towards the poles (Fig. 6b) and polarity-dependent velocity profiles (Extended Data Fig. 8). Similarly, when we reduced the motor activity in a gelled system, we observed the same polarity reversal (Fig. 6c).

Our simulations predict the possibility of an ‘inverted’ spindle phenotype when the motor activity is reduced or when the microtubule networks are not gelled. We tested the former by perturbing the spindles with the Eg5 inhibitor FCPT—a drug that suppresses Eg5 ATP hydrolysis—as well as keeping the motors bound to microtubules and thought to maintain spindle bipolarity⁴¹. In spindles, this drug abolished microtubule flows (Extended Data Fig. 9 and Supplementary Video 14) as well as maintained a spindle-like structure (Fig. 6e and Supplementary Video 15), in agreement with previous studies⁴¹. To test the possibility that FCPT treatment increases the lifetime of microtubules and thus the overall connectivity, we compared the microtubule lifetimes of FCPT-treated spindles to dynein-inhibited and control spindles, finding no clear differences (Extended Data Fig. 10). We, therefore, expect a similar filament connectivity in these treated spindles. According to our simulations, the abolition of microtubule flows in FCPT-treated spindles should trigger a microtubule polarity reversal, despite resembling regular spindles. When measuring microtubule polarity in these structures using laser ablation, we found a reversed microtubule polarity profile, with depolymerization waves propagating inwards (Supplementary Videos 15 and 16) instead of poleward (Supplementary Videos 17 and 18) (Fig. 6e,f). Altogether, these findings support that a gelation transition, together with molecular motor activity, is necessary for correct spindle self-organization.

A gelation transition enables the correct spindle architecture

By using a combination of laser ablation, speckle microscopy and simulations, we have shown that a gelation process in spindles can reverse the intrinsic polarity set by microtubule branching nucleation by means of long-range microtubule transport. Our results show that the generation of long-range flows in spindles requires that microtubules at the poles are sufficiently connected to primary microtubules in the region of productive antiparallel overlap in the spindle midplane where the forces are generated. This is evident

from our laser ablation experiments, where microtubule flows are severely impaired due to the disconnection of the spindle pole. One limitation of our laser ablation assay is that it cannot completely disentangle the contribution of rare long microtubules. Certainly, a small fraction of long microtubules spanning the midplane-to-pole region is present, and we cannot discard that they contribute to the generation of flows. However, as shown in our simulations, in the absence of gelation, long microtubules alone cannot account for the long-range flows. Instead, we hypothesize that they might help facilitate spindle gelation by establishing long connections within the microtubule networks. Overall, our results suggest that the gelation process is the key, and that connectivity is mediated by a percolated network of predominantly short microtubules that spans the full midplane-to-pole region. Our results are in line with recent studies showing that polarity-independent flows in nematic systems arise only in regimes of high cross-linking^{15,17}. Although the spindle was already known to be composed of two interdigitating antiparallel microtubule arrays with the plus ends of the microtubule pointing towards the chromosomal plate^{14,18,28,42–44}, it remained unclear how such an architecture could be reconciled with the presence of branching microtubule nucleation^{23,24,39}, which naturally leads to microtubule structures in which the plus ends of the microtubule point outwards. Our numerical simulations reveal that motor activity, together with a high degree of dynamic cross-linking, can reverse the polarity profile that would naturally result from autocatalytic microtubule nucleation in the proximity of chromosomes. We further tested this prediction by treating *Xenopus* egg extract spindles with the FCPT drug and observed a reversal of microtubule polarity. Hence, our study shows the key role of gelation in spindle assembly and highlights the important balance between autocatalytic microtubule nucleation, microtubule transport and cross-linking in organizing and maintaining the proper spindle architecture.

Online content

Any methods, additional references, Nature Research reporting summaries, source data, extended data, supplementary information, acknowledgements, peer review information; details of author contributions and competing interests; and statements of data and code availability are available at <https://doi.org/10.1038/s41567-021-01467-x>.

Received: 15 January 2021; Accepted: 12 November 2021;

Published online: 10 February 2022

References

- Howard, J. *Mechanics of Motor Proteins and the Cytoskeleton* (Sinauer Associates, 2001).
- Heisenberg, C.-P. & Bellaïche, Y. Forces in tissue morphogenesis and patterning. *Cell* **153**, 948–962 (2013).
- Miyamoto, D. T., Perlman, Z. E., Burbank, K. S., Groen, A. C. & Mitchison, T. J. The kinesin Eg5 drives poleward microtubule flux in *Xenopus laevis* egg extract spindles. *J. Cell Biol.* **167**, 813–818 (2004).
- Tolić-Nørrelykke, I. M. Push-me-pull-you: how microtubules organize the cell interior. *Eur. Biophys. J.* **37**, 1271–1278 (2008).
- Dumont, S. & Mitchison, T. J. Force and length in the mitotic spindle. *Curr. Biol.* **19**, R749–R761 (2009).
- Sanchez, T., Chen, D. T. N., DeCamp, S. J., Heymann, M. & Dogic, Z. Spontaneous motion in hierarchically assembled active matter. *Nature* **491**, 431–434 (2012).
- Mayer, M., Depken, M., Bois, J. S., Jülicher, F. & Grill, S. W. Anisotropies in cortical tension reveal the physical basis of polarizing cortical flows. *Nature* **467**, 617–621 (2010).
- Boukellal, H., Campás, O., Joanny, J.-F., Prost, J. & Sykes, C. Soft *Listeria*: actin-based propulsion of liquid drops. *Phys. Rev. E* **69**, 61906 (2004).
- Brugués, J., Nuzzo, V., Mazur, E. & Needleman, D. J. Nucleation and transport organize microtubules in metaphase spindles. *Cell* **149**, 554–564 (2012).
- Prost, J., Jülicher, F. & Joanny, J.-F. Active gel physics. *Nat. Phys.* **11**, 111–117 (2015).
- Mitchison, T. J. Polewards microtubule flux in the mitotic spindle: evidence from photoactivation of fluorescence. *J. Cell Biol.* **109**, 637–652 (1989).

12. Maddox, P., Desai, A., Oegema, K., Mitchison, T. J. & Salmon, E. D. Poleward microtubule flux is a major component of spindle dynamics and anaphase A in mitotic *Drosophila* embryos. *Curr. Biol.* **12**, 1670–1674 (2002).
13. Kapitein, L. C. et al. The bipolar mitotic kinesin Eg5 moves on both microtubules that it crosslinks. *Nature* **435**, 114–118 (2005).
14. Uteng, M., Hentrich, C., Miura, K., Bieling, P. & Surrey, T. Poleward transport of Eg5 by dynein–dynactin in *Xenopus laevis* egg extract spindles. *J. Cell Biol.* **182**, 715–726 (2008).
15. Striebel, M., Graf, I. R. & Frey, E. A mechanistic view of collective filament motion in active nematic networks. *Biophys. J.* **118**, 313–324 (2020).
16. Walczak, C. E., Vernos, I., Mitchison, T. J., Karsenti, E. & Heald, R. A model for the proposed roles of different microtubule-based motor proteins in establishing spindle bipolarity. *Curr. Biol.* **8**, 903–913 (1998).
17. Fürthauer, S. et al. Self-straining of actively crosslinked microtubule networks. *Nat. Phys.* **15**, 1295–1300, 2019.
18. Yang, G., Cameron, L. A., Maddox, P. S., Salmon, E. D. & Danuser, G. Regional variation of microtubule flux reveals microtubule organization in the metaphase meiotic spindle. *J. Cell Biol.* **182**, 631–639 (2008).
19. Needleman, D. J. et al. Fast microtubule dynamics in meiotic spindles measured by single molecule imaging: evidence that the spindle environment does not stabilize microtubules. *Mol. Biol. Cell* **21**, 323–333 (2010).
20. Redemann, S. et al. *C. elegans* chromosomes connect to centrosomes by anchoring into the spindle network. *Nat. Commun.* **8**, 15288 (2017).
21. Rieckhoff, E. M. et al. Spindle scaling is governed by cell boundary regulation of microtubule nucleation. *Curr. Biol.* **30**, 4973–4983 (2020).
22. Oh, D., Yu, C.-H. & Needleman, D. J. Spatial organization of the Ran pathway by microtubules in mitosis. *Proc. Natl Acad. Sci. USA* **113**, 8729–8734 (2016).
23. Decker, F., Oriola, D., Dalton, B. & Brugués, J. Autocatalytic microtubule nucleation determines the size and mass of *Xenopus laevis* egg extract spindles. *eLife* **7**, e31149 (2018).
24. Ishihara, K., Nguyen, P. A., Groen, A. C., Field, C. M. & Mitchison, T. J. Microtubule nucleation remote from centrosomes may explain how asters span large cells. *Proc. Natl Acad. Sci. USA* **111**, 17715–17722 (2014).
25. Kaye, B. et al. Measuring and modeling polymer concentration profiles near spindle boundaries argues that spindle microtubules regulate their own nucleation. *New J. Phys.* **20**, 55012 (2018).
26. Roostalu, J., Rickman, J., Thomas, C., Nédélec, F. & Surrey, T. Determinants of polar versus nematic organization in networks of dynamic microtubules and mitotic motors. *Cell* **175**, 796–808.e14 (2018).
27. Burbank, K. S., Mitchison, T. J. & Fisher, D. S. Slide-and-cluster models for spindle assembly. *Curr. Biol.* **17**, 1373–1383 (2007).
28. Loughlin, R., Heald, R. & Nédélec, F. A computational model predicts *Xenopus* meiotic spindle organization. *J. Cell Biol.* **191**, 1239–1249 (2010).
29. Oriola, D., Jülicher, F. & Brugués, J. Active forces shape the metaphase spindle through a mechanical instability. *Proc. Natl Acad. Sci. USA* **117**, 16154–16159 (2020).
30. Gaetz, J. & Kapoor, T. M. Dynein/dynactin regulate metaphase spindle length by targeting depolymerizing activities to spindle poles. *J. Cell Biol.* **166**, 465–471 (2004).
31. Rogers, G. C., Rogers, S. L. & Sharp, D. J. Spindle microtubules in flux. *J. Cell Sci.* **118**, 1105–1116 (2005).
32. Oriola, D., Needleman, D. J. & Brugués, J. The physics of the metaphase spindle. *Annu. Rev. Biophys.* **47**, 655–673 (2018).
33. Crocker, J. C. et al. Two-point microrheology of inhomogeneous soft materials. *Phys. Rev. Lett.* **85**, 888 (2000).
34. Brugués, J. & Needleman, D. Physical basis of spindle self-organization. *Proc. Natl Acad. Sci. USA* **111**, 18496–18500 (2014).
35. Thorpe, M. F. and Duxbury, P. M. *Rigidity Theory and Applications* (Springer Science & Business Media, 1999).
36. Alvarado, J., Sheinman, M., Sharma, A., MacKintosh, F. C. & Koenderink, G. H. Molecular motors robustly drive active gels to a critically connected state. *Nat. Phys.* **9**, 591–597 (2013).
37. Alvarado, J., Sheinman, M., Sharma, A., MacKintosh, F. C. & Koenderink, G. H. Force percolation of contractile active gels. *Soft Matter* **13**, 5624–5644 (2017).
38. Shimamoto, Y., Maeda, Y. T., Ishiwata, S., Libchaber, A. J. & Kapoor, T. M. Insights into the micromechanical properties of the metaphase spindle. *Cell* **145**, 1062–1074 (2011).
39. Petry, S., Groen, A. C., Ishihara, K., Mitchison, T. J. & Vale, R. D. Branching microtubule nucleation in *Xenopus* egg extracts mediated by augmin and TPX2. *Cell* **152**, 768–777 (2013).
40. Ishihara, K., Korolev, K. S. & Mitchison, T. J. Physical basis of large microtubule aster growth. *Elife* **5**, e19145 (2016).
41. Groen, A. C. et al. A novel small-molecule inhibitor reveals a possible role of kinesin-5 in anastral spindle-pole assembly. *J. Cell Sci.* **121**, 2293–2300 (2008).
42. Sharp, D. J., Rogers, G. C. & Scholey, J. M. Microtubule motors in mitosis. *Nature* **407**, 41–47 (2000).
43. Alberts, B., Wilson, J. & Hunt, T. *Molecular Biology of the Cell* (Garland Science, 2008).
44. Takagi, J., Sakamoto, R., Shiratsuchi, G., Maeda, Y. T. & Shimamoto, Y. Mechanically distinct microtubule arrays determine the length and force response of the meiotic spindle. *Dev. Cell* **49**, 267–278 (2019).

Publisher's note Springer Nature remains neutral with regard to jurisdictional claims in published maps and institutional affiliations.



Open Access This article is licensed under a Creative Commons Attribution 4.0 International License, which permits use, sharing, adaptation, distribution and reproduction in any medium or format, as long as you give appropriate credit to the original author(s) and the source, provide a link to the Creative Commons license, and indicate if changes were made. The images or other third party material in this article are included in the article's Creative Commons license, unless indicated otherwise in a credit line to the material. If material is not included in the article's Creative Commons license and your intended use is not permitted by statutory regulation or exceeds the permitted use, you will need to obtain permission directly from the copyright holder. To view a copy of this license, visit <http://creativecommons.org/licenses/by/4.0/>.

© The Author(s) 2022

Methods

Cytoplasmic extract preparation, spindle assembly and biochemical perturbations.

Cytostatic factor (CSF)-arrested *X. laevis* egg extract was prepared as described previously^{35,46}. In brief, unfertilized frog eggs were dejellied and crushed by centrifugation. After adding protease inhibitors (leupeptin, pepstatin and chymostatin (LPC)) and cytochalasin D (CyD) to a final concentration of 10 $\mu\text{g ml}^{-1}$ each to the fresh extract, we cycled single reactions to the interphase by adding frog sperm (to a final concentration of 300–1,000 sperm μl^{-1}) and calcium solution (10.0 mM CaCl_2 , 250.0 mM KCl and 2.5 mM MgCl_2 to a final concentration of 0.4 mM Ca^{++}), with a subsequent incubation of 1.5 h. Although fresh CSF extract containing LPC and CyD was kept on ice, all the incubation steps were performed at 18–20 °C. The reactions were driven back into the metaphase by adding 1.3 volumes of fresh CSF extract (containing LPC and CyD). The spindles formed within 30 min of incubation. We inhibited dynein with $\sim 10 \mu\text{M}$ p150-CC1 (purified according to King et al.⁴⁷) and Eg5 using $\sim 100 \mu\text{M}$ FCPT. In both cases, inhibitors were added to the reactions and incubated for an additional ~ 20 min. Before imaging, Atto565-labelled purified porcine tubulin (purified according to Castoldi et al.⁴⁸) and Hoechst 33342 were added to the reactions to a final concentration of 150 nM and $\sim 16 \mu\text{g ml}^{-1}$, respectively, to visualize the microtubules and DNA. For speckle microscopy experiments, Atto565 frog tubulin (purified from *X. laevis* frog egg extract according to Groen et al.⁴⁹) was added to the egg extracts to a final concentration of ~ 1 nM. The speckle videos were obtained from distinct spindles on different extract days.

Image acquisition. Fluorescent spindles were imaged using a Nikon spinning-disc microscope (ECLIPSE Ti), electron-multiplying charge-coupled device camera (Andor iXon DU-888), $\times 60$ 1.2 numerical aperture water-immersion objective and AndorIQ software for image acquisition. The room temperature was kept at 19 °C.

Microtubule lifetime measurements. The speckles were tracked using the Fiji plugin TrackMate⁵⁰, and the resulting track statistics were analysed with a custom-written Python (3.8) code. We included only those speckles that appeared and disappeared during the length of the video. To calculate the average lifetime of the microtubules, we used the lifetime distribution $P(t)$ of a diffusion and drift process to fit it to our data according to $P(t) \approx t^{-3/2} e^{-t/\tau}$, where $\tau/4$ is the expected lifetime of a microtubule of average length¹⁹.

Laser ablation. The femtosecond laser ablation setup was composed of a mode-locked Ti:sapphire laser (Coherent Chameleon Vision II) oscillator coupled into the back port of the Nikon spinning-disc microscope and delivering 140 fs pulses at a repetition rate of 80 MHz. We used a pulse picker (APE pulseSelect) to reduce the pulse frequency to 20 kHz. Cutting was performed using a wavelength of 800 nm; typically, power of $\sim 500 \mu\text{W}$ was used before the objective. The sample was mounted on a piezo stage that positioned the sample in three dimensions with sub-micrometre precision. The laser-cutting process was automatically executed by a custom-written software that controlled the mechanical shutter in the beam path and moved the piezo stage to create the desired shape of the cut. Linear cuts were performed in several planes to cover the total depth of the spindle around the focal plane. The density of cuts in depth was two cuts per micrometre to ensure proper disconnection of the spindle. Cutting was finished within 2–10 s depending on the thickness of the cut region. The images were acquired at least every 2 s during the cutting procedure as well as for ~ 3 min after the cut. The depolymerization wave typically disappeared within 30 s. The laser cuts were performed a maximum of three times on the same spindle. The analysis of the spindle cuts was done using custom C++ (Microsoft Visual C++ 2012 Redistributable (x64) 11.0.61030) and Python scripts.

Simulation of active long-range flows. All the simulations were performed using custom simulation software, which is available for download. The simulations included filament nucleation and turnover, as well as active-force generation by transient motors that walked along the filaments mimicking Eg5 (Supplementary Information provides a schematic with an overview). In the pinning-field channel simulations, new filaments are nucleated with an orientation that is antiparallel to the pinning field. Eg5 performed the roles of both cross-linker in parallel overlaps and a motor in antiparallel overlaps. The mean lifetime for the dynamic filaments was approximately 30 s and the mean pair-binding time for the Eg5 motors was 10 s. To ensure a high filament density as well as to reproduce the conditions for microtubule orientation in the spindle, we confined the filaments to narrow channels with strongly repulsive walls that forced the filaments into a dense polar phase (Extended Data Fig. 4). This minimal system enabled us to study how localized active stresses can propagate through cross-linked filament networks. Pinning-field channel simulations are described in Supplementary Information. The channel cross-section is 1 μm in both the x and y directions. The domain of nucleation is between $z=0$ and 75 μm . The average number of microtubules in the steady state is approximately 530 with a mean length of 6.5 μm (Extended Data Fig. 4a). We varied the number of available motors for each state point. In the steady state, the average number of pair-bound motors is constant (Extended Data Fig. 4b). For the long, narrow channel simulations (Fig. 4d–g), the steady-state number of pair-bound motors reads 25, 80, 170, 315, 530, 960, 2,260, 4,875 and 7,770. For the short, wide channel simulations (Fig. 4h–i), the range reads 550, 2,330 and 3,760. The simulations were typically run

for 5×10^8 time steps with individual time steps representing $\Delta t = 5 \mu\text{s}$. We allowed 1×10^8 time steps for the system to reach a steady state before collecting the data. The data were collected every 1×10^5 time steps (0.5 s). For the velocity profiles, we calculated the displacements every 2 s. For correlation calculations, we calculated the fluctuations with time steps of 4 s. For each state point, we reduced the noise by averaging over ten simulations with the same microscopic parameters but initiated with different random seeds. The plotted velocity profiles and correlation profiles correspond to the mean over the ten simulations. The error bars correspond to standard deviations. We describe the details for calculating the velocity profiles, connectivity plots and correlations in detail in Supplementary Information. We carried out all the analyses using custom MATLAB (version R2018a) scripts.

Active microrheology simulations. We describe the simulations to probe the material properties of our system in detail in Supplementary Information. To avoid active flows, we set the motor velocity to zero. Otherwise, the cross-linker parameters correspond to the same used for Eg5. For each oscillation frequency and cross-linker concentration, we averaged over ten simulations. We allowed 3.5×10^8 time steps before beginning the pinning-field oscillations. Once the oscillations begun, the simulations were run for long enough such that a minimum of four oscillation cycles could be completed. We discarded the data from the first cycle to avoid transient effects. The domain of microtubule nucleation is found between $z=0$ and 40 μm . On average, approximately 300 dynamic microtubules exist in the steady state. The number of pair-bound cross-linkers corresponds to 410, 850, 1,280, 1,710, 2,550 and 5,070. We set the equilibrium trap position at $z=20 \mu\text{m}$ and the stable, trapped filament had a constant length of 7 μm . We chose oscillation frequencies such that we could best probe the viscous and elastic response for different cross-linker concentrations. Thus, we used oscillation periods of 10, 30, 45, 60, 120, 180 and 300 s, all of them with an amplitude of $z_0 = 0.75 \mu\text{m}$. We recorded and analysed the trajectories for the trapped filaments using custom MATLAB scripts.

Branching filament network simulations. Branching simulations are described in detail in Supplementary Information. The initial conditions for all the simulations shown in Fig. 6 and Extended Data Fig. 6, except for Extended Data Fig. 6c, are from two seeds of opposite polarity, with the centre of mass of the filament located at $z(t=0) = -4 \mu\text{m}$ and $4 \mu\text{m}$ (or $-3 \mu\text{m}$ and $3 \mu\text{m}$; Fig. 6a), with the plus ends pointing towards each other. In Extended Data Fig. 7, we consider a system generated with an alternative initial condition. In general, to spatially localize the nucleation, branching nucleation is restricted to occur on the filament sites that are located between the channel positions $z = -8 \mu\text{m}$ and $8 \mu\text{m}$ (except for Extended Data Fig. 6c). This is intended to represent the length scale of the branching nucleation activity. Figure 6a shows the transient, early-stage development of the simulated system, and is intended for visualization purposes. The polarity profiles displayed below the simulation snapshots in Fig. 6a are instantaneous profiles for the networks presented at $t=60$ s. Systems evolve until a steady state is reached, requiring approximately 150 s (Extended Data Fig. 6d–g). Once in the steady state, we recorded the density and polarity profiles. For each state point, we run ten individual simulations with equivalent microscopic parameters and initial conditions, but with different random number generator seeds. The error bars in Fig. 6b–d correspond to standard deviations for the instantaneous polarity and density profiles, taken across the ten individual simulations. The error bars in Extended Data Figs. 6c–e and 7e,f were calculated in the same way. The branching nucleation rate, number of available nucleators and catastrophe rate resulted in a steady-state value of approximately 500 filaments in total (sum of both networks). The steady-state values for the number of pair-bound motors correspond to 0, 175, 385, 800 and 1,225, resulting in ratios of the number of motors to the number of filaments of approximately 0, 0.36, 0.77, 1.60 and 2.50. Extended Data Fig. 6c shows the time evolution of a system with the initial condition of a single filament seed, located at $z=0 \mu\text{m}$ and with initial orientation $u_z = 1$, an unbounded domain of nucleation, and a limited number of available nucleators.

Reporting Summary. Further information on research design is available in the Nature Research Reporting Summary linked to this article.

Data availability

All the data generated or analysed in this study are available from the corresponding authors upon reasonable request.

Code availability

All the computer simulations and data analysis were performed using custom MATLAB, C++ or Python code. Particle tracking was performed using the ImageJ plugin TrackMate from Fiji. The computer simulation software can be downloaded from the Zenodo website (<https://doi.org/10.5281/zenodo.4618598>). Additional codes to analyse the data are available from the corresponding authors upon reasonable request.

References

- Murray, A. W. Cell cycle extracts. *Methods Cell Biol.* **36**, 581–605 (1991).
- Hannak, E. & Heald, R. Investigating mitotic spindle assembly and function in vitro using *Xenopus laevis* egg extracts. *Nat. Protoc.* **1**, 2305–2314 (2006).

47. King, S. J., Brown, C. L., Maier, K. C., Quintyne, N. J. & Schroer, T. A. Analysis of the dynein-dynactin interaction in vitro and in vivo. *Mol. Biol. Cell* **14**, 5089–5097 (2003).
48. Castoldi, M. & Popov, A. V. Purification of brain tubulin through two cycles of polymerization–depolymerization in a high-molarity buffer. *Protein Expr. Purif.* **32**, 83–88 (2003).
49. Groen, A. C. and Mitchison, T. J. *Purification and Fluorescent Labeling of Tubulin from *Xenopus laevis* Egg Extracts* 35–45 (Springer, 2016).
50. Tinevez, J.-Y. et al. TrackMate: an open and extensible platform for single-particle tracking. *Methods* **115**, 80–90 (2017).

Acknowledgements

We thank K. Ishihara for providing the construct to purify the p150-CC1 protein. We acknowledge J. Pelletier and T. Mitchison for kindly providing us the FCPT inhibitor, and M. Loose for useful discussions and feedback on the paper. We thank all the members of the Brugués Lab for discussions and H. Andreas for frog maintenance. We acknowledge funding from EMBO (Long-Term Fellowship with number 483-2016 to D.O.) and HFSP (CDA 74/2014 to J.B.). B.A.D. was supported by an ELBE Postdoctoral Fellowship from the CSBD.

Author contributions

B.A.D., D.O. and F.D. contributed equally to this work. B.A.D., D.O., F.D. and J.B. conceived the project. B.A.D. performed the computer simulations and theoretical

research. D.O. performed the theoretical and experimental research and analysed the experimental data. F.D. performed the experimental research and analysed the experimental data. All the authors drafted the manuscript. J.B. and F.J. directed the project.

Funding

Open access funding provided by Max Planck Society.

Competing interests

The authors declare no competing interests.

Additional information

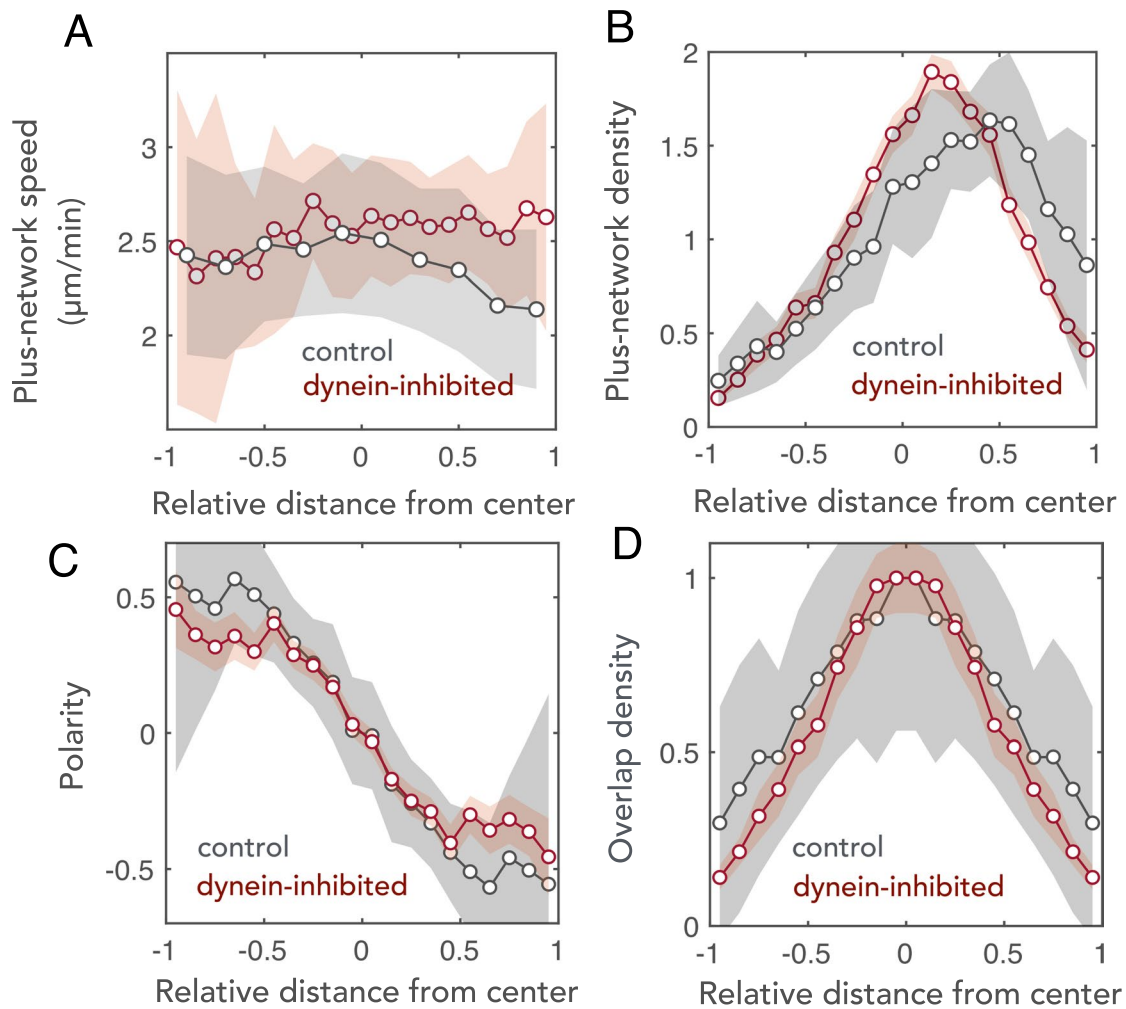
Extended data is available for this paper at <https://doi.org/10.1038/s41567-021-01467-x>.

Supplementary information The online version contains supplementary material available at <https://doi.org/10.1038/s41567-021-01467-x>.

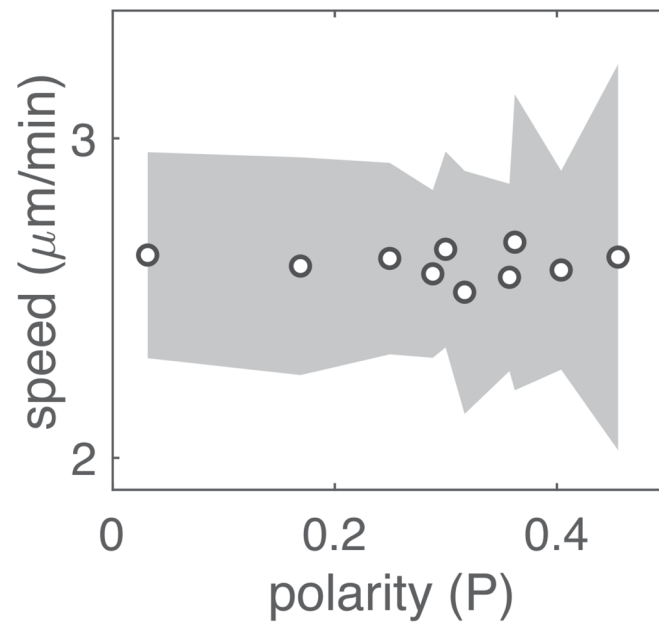
Correspondence and requests for materials should be addressed to Frank Jülicher or Jan Brugués.

Peer review information *Nature Physics* thanks Jennifer Ross and the other, anonymous, reviewer(s) for their contribution to the peer review of this work.

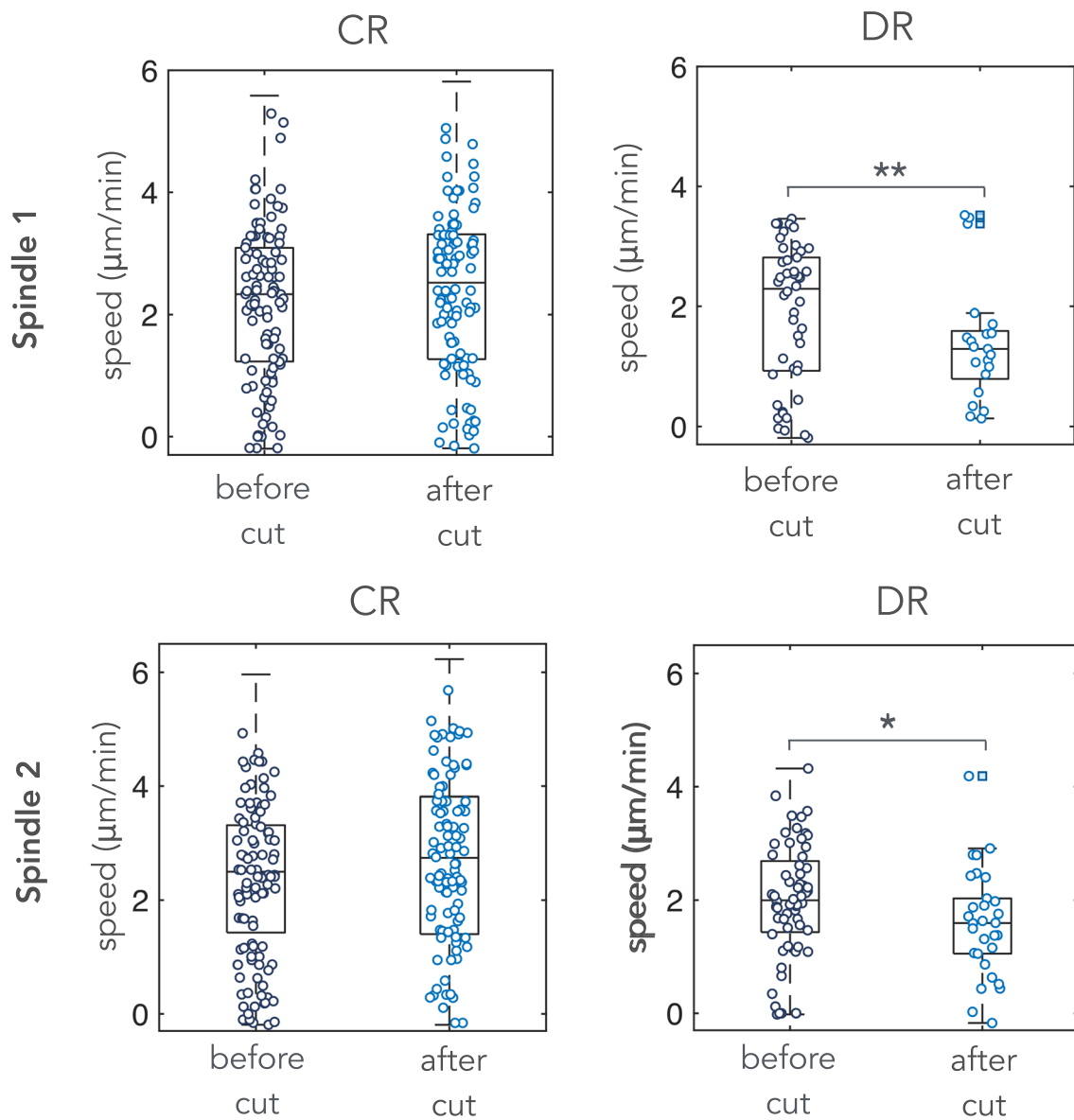
Reprints and permissions information is available at www.nature.com/reprints.



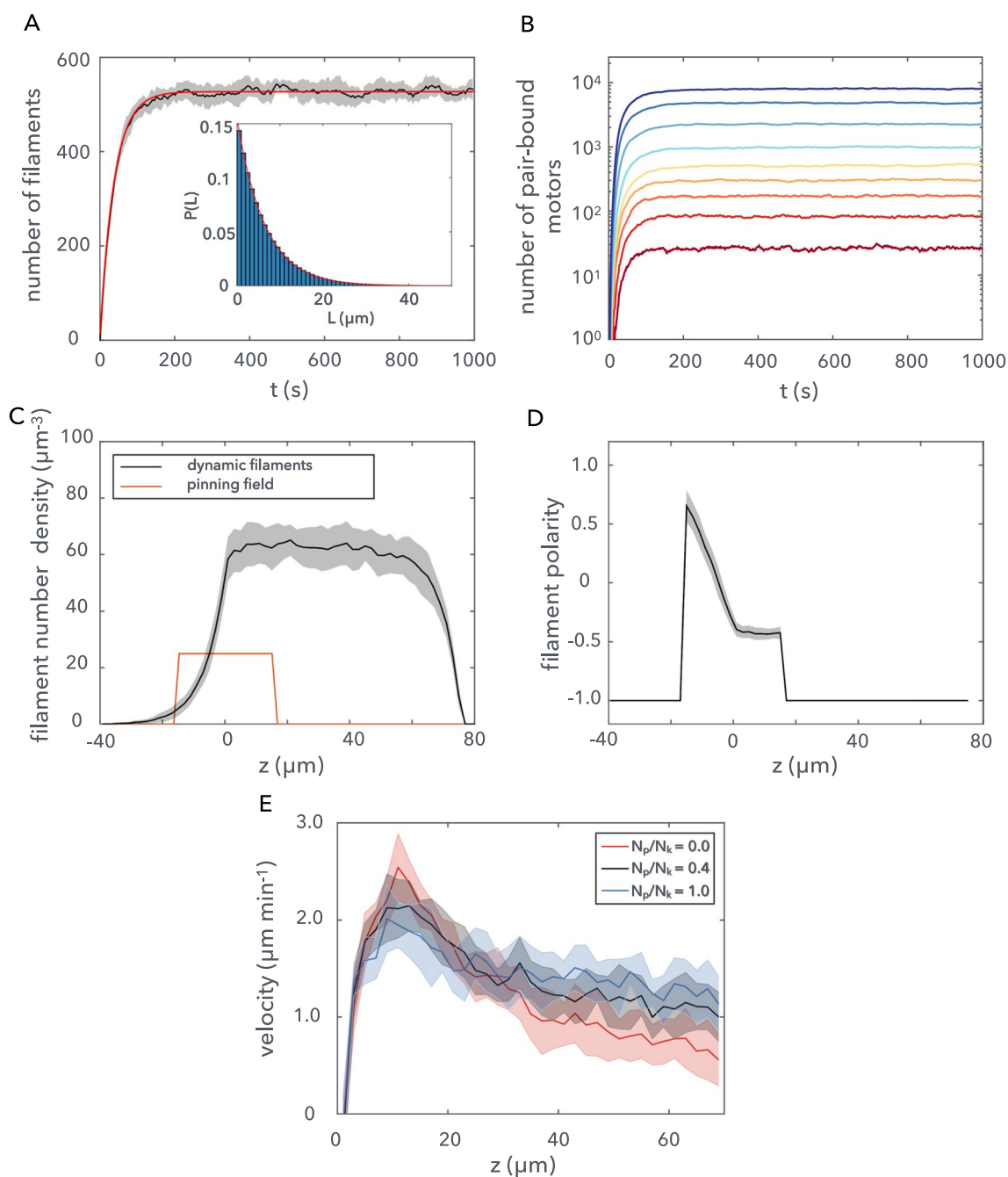
Extended Data Fig. 1 | Microtubule architecture of control and dynein-inhibited spindles. Comparison between the microtubule architecture of control ($n=13$ spindles, black) and dynein-inhibited spindles ($n=10$ spindles, red; data from Fig. 1). (A) Averaged velocity profiles of the plus-network. (B) Density profiles of the plus-network. (C) Polarity profiles. (D) Antiparallel overlap densities. Gray shaded areas indicate SD.



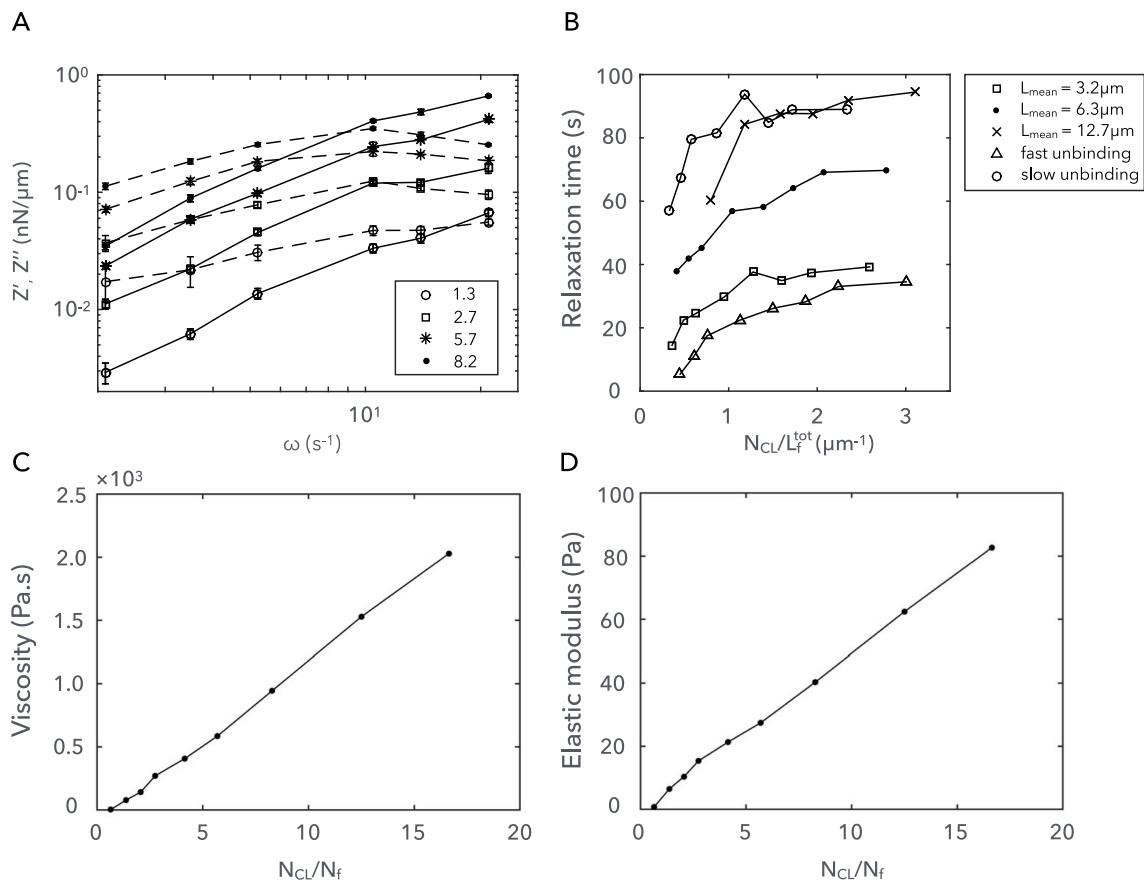
Extended Data Fig. 2 | Microtubule transport velocity does not depend on microtubule polarity. Microtubule transport velocity vs polarity using the data in Fig. 1. Shaded error bars correspond to the SD.



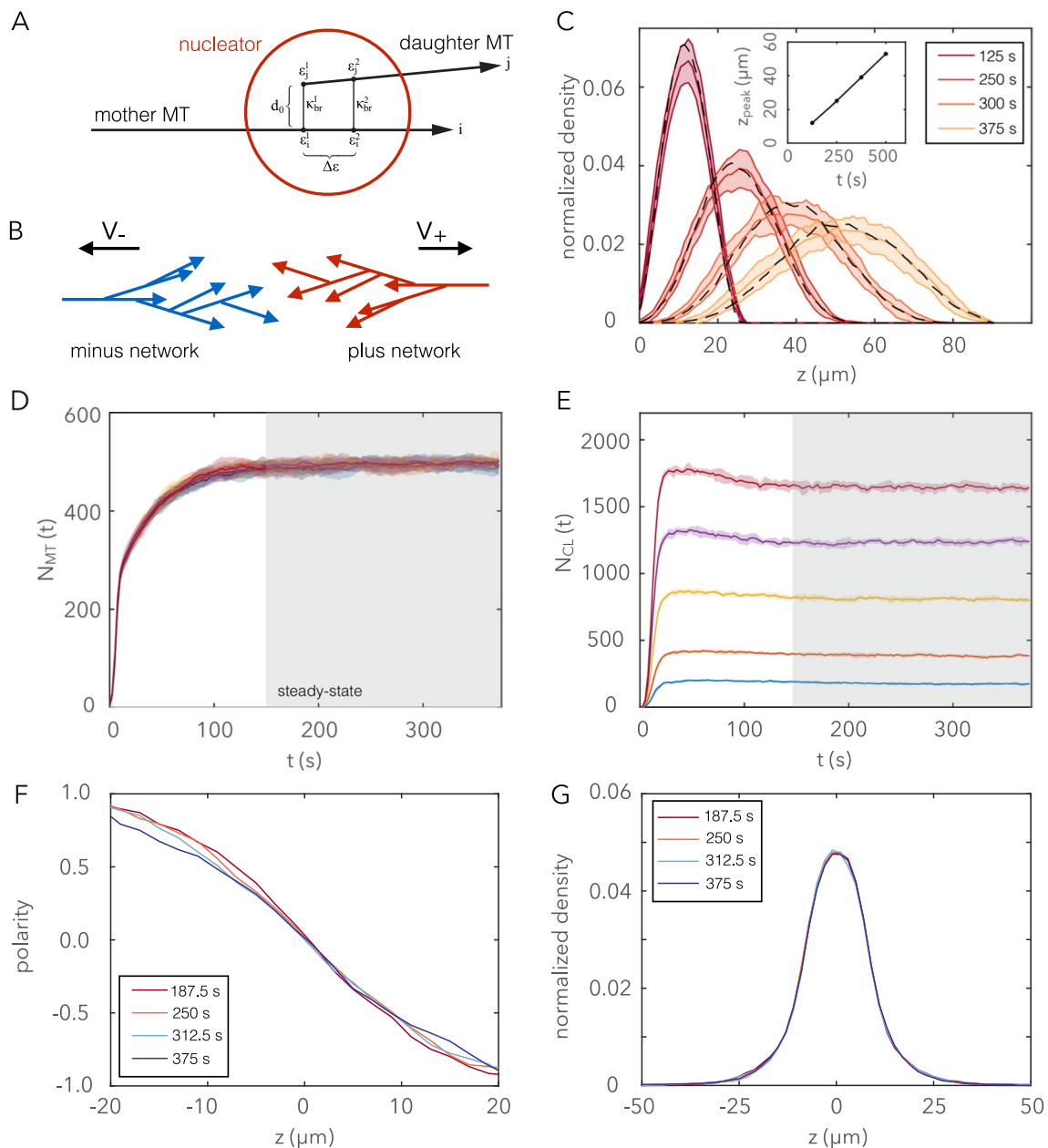
Extended Data Fig. 3 | Additional data for speckle velocities before and after pole disconnection. Box plots of the average on-axis velocity of speckles before and after cuts for connected (CR) and disconnected (DR) regions. Only speckles with $> -0.2 \mu\text{m}/\text{min}$ were considered in the analysis. A reduced subset of 100 data points is shown in the disconnected region case for the sake of clarity. * $p < 0.05$ and ** $p < 0.01$. Squares indicate outliers. The test used was a two-sample t-test. Spindle 1 corresponds to Supplementary Video 10, and Spindle 2 corresponds to Supplementary Video 11.



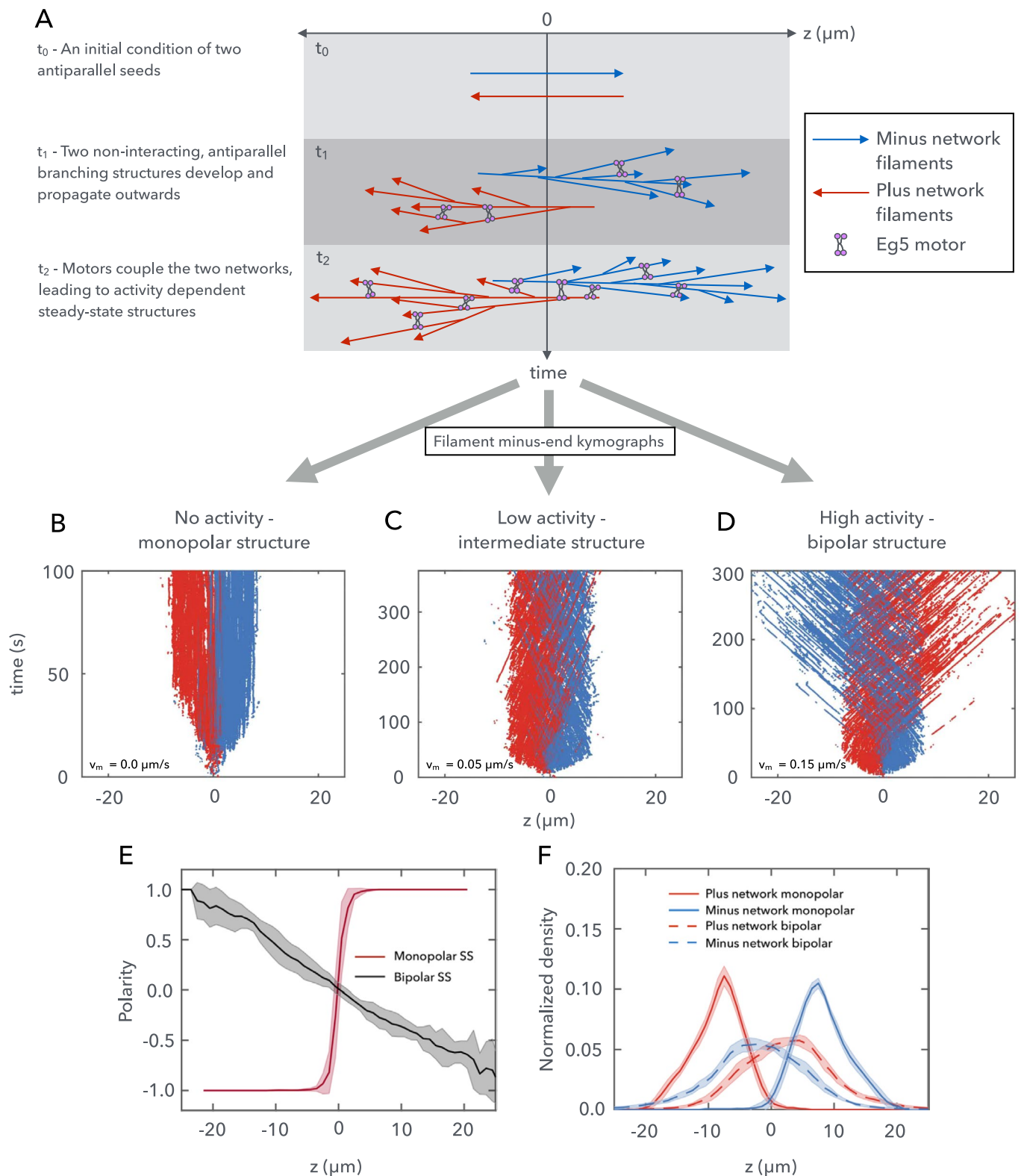
Extended Data Fig. 4 | Additional details for pinning-field channel simulations. (A) Mass turnover of dynamic filaments. The trajectory in black shows $\langle N(t) \rangle$ averaged over 10 simulations with standard deviations. The red curve shows a theoretical prediction given by $N(t) = k_n \tau (1 - \exp(-t/\tau))$, where $\tau = (1 + v_+/v_-)/k_c$ is the mean filament lifetime, k_c is the catastrophe rate and k_n is the nucleation rate, and v_+ and v_- are the polymerization and depolymerization rates of the filaments respectively. (Inset) filament length distribution with exponential fit (red curve) (mean length $6.5 \mu\text{m}$). (B) The number of pair-bound Eg5 motors as a function of time, corresponding to Figs. 1d-g. (C) The number density for the two distinct filament populations, calculated along the length of the pinning-field channel. The finite domain of nucleation is between $z=0$ and $75 \mu\text{m}$. (D) The total filament polarity profile, combining dynamic filaments and the pinning field. $n=10$ simulations, mean \pm SD. (E) Velocity profiles for systems with mixed Eg5 and passive cross-linkers (zero velocity), for moderate concentrations of Eg5 motors. Number of available Eg5 motors is $N_k = 350$ for all systems. N_p is the number of passive cross-linkers. Otherwise, relevant parameters for passive motors are chosen to be the same as Eg5, as given in Table 2 of the Supplementary Information.



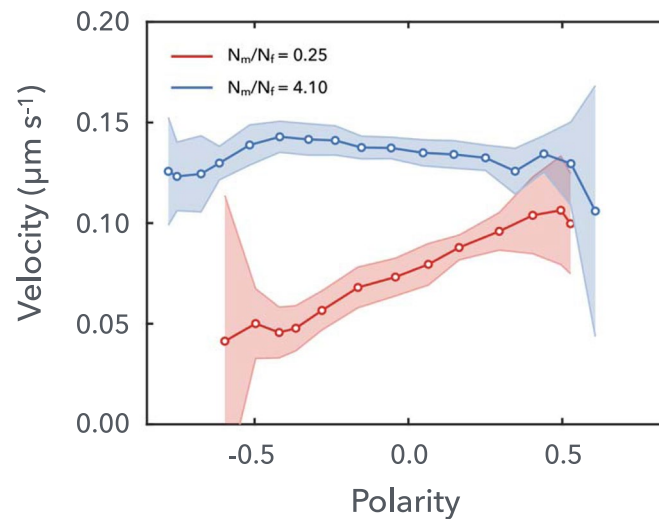
Extended Data Fig. 5 | Active microrheology and material properties of simulated filament networks. (A) Four examples of viscoelastic response, calculated with AMR. The intercept of the solid response (bold line) and the fluid response (dashed line) indicates the scaling frequency and modulus, used to scale each system for Fig. 5e. The figure legend presents N_{cl}/N_f , as in Fig. 5e. (B) Relaxation times calculated using the AMR technique for different system parameters. The dependency on filament length distribution and the crosslinker unbinding rate is shown. The independent variable is N_{cl}/L_f^{tot} since L_f^{tot} will be the same for each system with equal crosslinker concentration, whereas N_{cl}/N_f will vary, depending on the microtubule length distribution. Motor binding and unbinding parameters for the fast unbinding system are $k_{on} = 2.5 \times 10^{-4} \mu\text{m}^{-1} \text{s}^{-1}$ and $k_{off} = 0.1 \text{s}^{-1}$, and for the slow unbinding system $k_{on} = 2.5 \times 10^{-4} \mu\text{m}^{-1} \text{s}^{-1}$ and $k_{off} = 0.011 \text{s}^{-1}$. Effective network viscosity (C) and elastic modulus (D) calculated using AMR (Supplementary Information: Active microrheology).



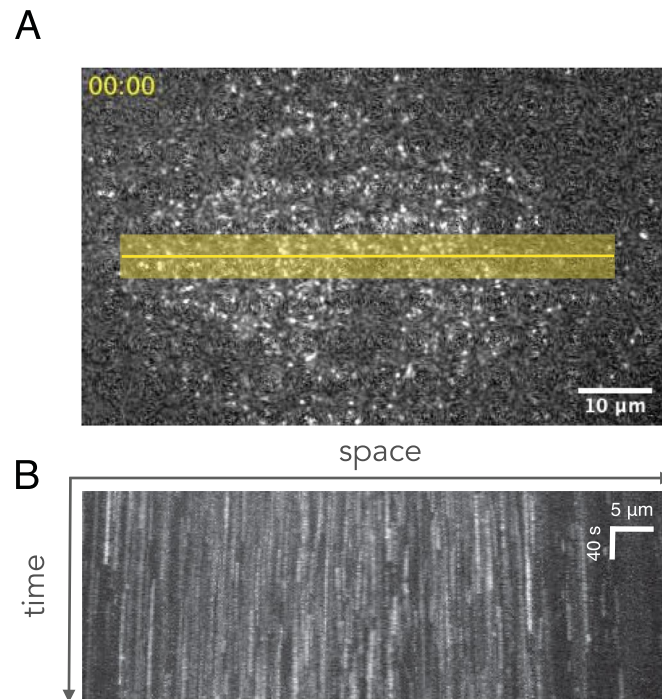
Extended Data Fig. 6 | Additional details for branching filament network simulations. (A) Schematic showing the branching connections introduced by a nucleation event. Descriptions of the various parameters are found in the Supplementary Information: branching nucleation. (B) Plus and minus network naming conventions. Naming indicates the direction of active transport due to Eg5 activity. (C) Forward autocatalytic propagation of a single branching network along a channel. Branching nucleation can occur in the domain $0 < z < 100 \mu\text{m}$. Networks begin from a single seed. A finite number of nucleators places an upper limit on the total mass density. Nucleation rate $0.1 \mu\text{m}^{-1}\text{s}^{-1}$. Black dashed line for nucleation rate $1.0 \mu\text{m}^{-1}\text{s}^{-1}$. (inset) mass density peak location as a function of time. The velocity of peak propagation is $\sim 0.1 \mu\text{m}\text{s}^{-1}$. (D), (E), and (F) details of the system steady-state for data shown in the main text Fig. 6. (D) Evolution of the number of filaments for Fig. 6b-d. Grey region indicates the steady-state where the total mass saturates. (E) Number of crosslinkers (Eg5) in Fig. 6c. (F) and (G) Instantaneous polarity and density profiles for the two interacting branching networks shown at different time intervals in the steady-state region.



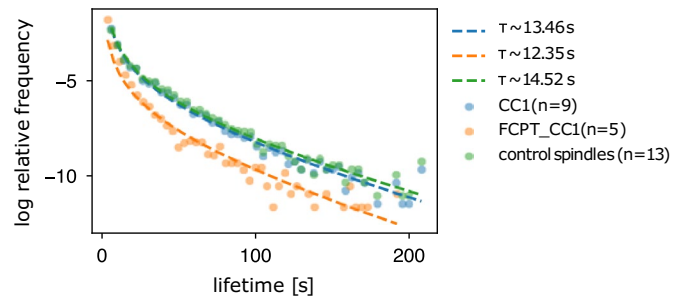
Extended Data Fig. 7 | Branching filament network simulations generate robust steady-states for non-trivial initial conditions. (A) Schematic showing antiparallel seed initial conditions and early-stage development of branching networks. Two antiparallel seeds spawn branched filament networks (t_0), which do not initially interact (t_1). After some time (t_2), the two networks may approach each other such that Eg5 can couple the two networks. The subsequent dynamics depend on Eg5 motor activity. (B) - (D) Filament minus-end kymographs generated from simulation trajectories with different motor activities. (E) Polarity calculated for steady-state monopolar structure (B at $t=100$ s) and bipolar structure (D at $t=300$ s). (F) Steady-state normalized filament mass density for the distinct plus and minus networks. Polarity and density are averaged over $n=10$ simulations at the same time point, with mean \pm SD. We neglect systems that remain uncoupled by Eg5 from our analysis.



Extended Data Fig. 8 | Gelation enables polarity-independent flows in simulated spindles. Plus-network velocities for branching filament network simulations above and below the gelation transition. Velocities are calculated from speckle points that are random and uniformly distributed along filaments. Steady-state dynamics are expected after approximately $t=200$ s. Velocity and polarity histograms are accumulated between $t=250$ s and $t=325$ s. $n=15$ for each N_m/N_f , with mean \pm SD for the velocity. Errors are excluded for polarity. Eg5 motor velocity is $v_m = 0.15 \mu\text{m s}^{-1}$. All rate parameters are the same as in Fig. 6 and Extended Data Fig. 6 (see Tables 1 and 2 in the Supplementary Information).



Extended Data Fig. 9 | Spindle polarity reversal as a consequence of FCPT treatment. (A) Speckle microscopy snapshot of a spindle inhibited with $-100\mu\text{M}$ FCPT and $-10\mu\text{M}$ p150-cc1. The image corresponds to the first time point of Supplementary Video 14. (B) Kymograph along the yellow line in (A) showing that microtubule transport is abolished.



Extended Data Fig. 10 | FCPT-treatment does not change microtubule lifetime. Microtubule speckles were tracked using the Fiji-plugin TrackMate and their lifetimes fitted using the equation published in Ref. ¹⁹. The expected microtubule lifetime τ , for a microtubule of average length is given for each fit. The number of analyzed spindles per condition n , is given in parentheses.

Reporting Summary

Nature Research wishes to improve the reproducibility of the work that we publish. This form provides structure for consistency and transparency in reporting. For further information on Nature Research policies, see our [Editorial Policies](#) and the [Editorial Policy Checklist](#).

Statistics

For all statistical analyses, confirm that the following items are present in the figure legend, table legend, main text, or Methods section.

n/a Confirmed

- The exact sample size (n) for each experimental group/condition, given as a discrete number and unit of measurement
- A statement on whether measurements were taken from distinct samples or whether the same sample was measured repeatedly
- The statistical test(s) used AND whether they are one- or two-sided
Only common tests should be described solely by name; describe more complex techniques in the Methods section.
- A description of all covariates tested
- A description of any assumptions or corrections, such as tests of normality and adjustment for multiple comparisons
- A full description of the statistical parameters including central tendency (e.g. means) or other basic estimates (e.g. regression coefficient) AND variation (e.g. standard deviation) or associated estimates of uncertainty (e.g. confidence intervals)
- For null hypothesis testing, the test statistic (e.g. F , t , r) with confidence intervals, effect sizes, degrees of freedom and P value noted
Give P values as exact values whenever suitable.
- For Bayesian analysis, information on the choice of priors and Markov chain Monte Carlo settings
- For hierarchical and complex designs, identification of the appropriate level for tests and full reporting of outcomes
- Estimates of effect sizes (e.g. Cohen's d , Pearson's r), indicating how they were calculated

Our web collection on [statistics for biologists](#) contains articles on many of the points above.

Software and code

Policy information about [availability of computer code](#)

Data collection Image acquisition was done using a Nikon spinning disk microscope (TI Eclipse), an EMCCD camera (Andor iXon DU-888) and the software AndorIQ. Simulations were performed using custom software written in C++, which can be downloaded from the following Zenodo repository: <https://doi.org/10.5281/zenodo.4618598>.

Data analysis All computer simulations and data analysis were performed using custom MATLAB, Python and C++ software. Particle tracking was performed using the ImageJ plugin TrackMate from Fiji. All simulation and data analysis software is available from the authors on request.

For manuscripts utilizing custom algorithms or software that are central to the research but not yet described in published literature, software must be made available to editors and reviewers. We strongly encourage code deposition in a community repository (e.g. GitHub). See the Nature Research [guidelines for submitting code & software](#) for further information.

Data

Policy information about [availability of data](#)

All manuscripts must include a [data availability statement](#). This statement should provide the following information, where applicable:

- Accession codes, unique identifiers, or web links for publicly available datasets
- A list of figures that have associated raw data
- A description of any restrictions on data availability

Figures 1, 2, 3, and 6 contain data generated using spinning disk microscopy. Figures 4, 5, and 6 contain data generated using computer simulation. The raw data is available from the authors on request.

Field-specific reporting

Please select the one below that is the best fit for your research. If you are not sure, read the appropriate sections before making your selection.

Life sciences Behavioural & social sciences Ecological, evolutionary & environmental sciences

For a reference copy of the document with all sections, see [nature.com/documents/nr-reporting-summary-flat.pdf](https://www.nature.com/documents/nr-reporting-summary-flat.pdf)

Life sciences study design

All studies must disclose on these points even when the disclosure is negative.

Sample size	The number of measurements done in this study (laser cuts, speckle tracks, etc) were sufficient to obtain statistically significant results and clear spatio-temporal profiles.
Data exclusions	No data was excluded from the study.
Replication	The experiments were independently conducted by two different authors. Replicates were done in different days, collecting eggs from different frogs.
Randomization	Not relevant to our study. Samples were not affected by randomization.
Blinding	Whenever possible, data collection and analysis was done independently by more than one author.

Reporting for specific materials, systems and methods

We require information from authors about some types of materials, experimental systems and methods used in many studies. Here, indicate whether each material, system or method listed is relevant to your study. If you are not sure if a list item applies to your research, read the appropriate section before selecting a response.

Materials & experimental systems

n/a	Involvement in the study
<input checked="" type="checkbox"/>	<input type="checkbox"/> Antibodies
<input checked="" type="checkbox"/>	<input type="checkbox"/> Eukaryotic cell lines
<input checked="" type="checkbox"/>	<input type="checkbox"/> Palaeontology and archaeology
<input type="checkbox"/>	<input checked="" type="checkbox"/> Animals and other organisms
<input checked="" type="checkbox"/>	<input type="checkbox"/> Human research participants
<input checked="" type="checkbox"/>	<input type="checkbox"/> Clinical data
<input checked="" type="checkbox"/>	<input type="checkbox"/> Dual use research of concern

Methods

n/a	Involvement in the study
<input checked="" type="checkbox"/>	<input type="checkbox"/> ChIP-seq
<input checked="" type="checkbox"/>	<input type="checkbox"/> Flow cytometry
<input checked="" type="checkbox"/>	<input type="checkbox"/> MRI-based neuroimaging

Animals and other organisms

Policy information about [studies involving animals](#); [ARRIVE guidelines](#) recommended for reporting animal research

Laboratory animals	Xenopus laevis (Nasco), male and female.
Wild animals	The study did not involve wild animals.
Field-collected samples	The study did not involve samples collected from the field.
Ethics oversight	All animals were handled according to the directive 2010/63/EU on the protection of animals used for scientific purposes, and the German animal welfare law under the license document number DD24-5131/367/9 from the Landesdirektion Sachsen (Dresden) - Section 24D.

Note that full information on the approval of the study protocol must also be provided in the manuscript.